Timing and provenance of volcanic fluxes around the Permian-Triassic Boundary Mass Extinction in South China: U-Pb zircon geochronology, volcanic ash geochemistry and mercury isotopes

Oluwaseun Edward[1], André Navin Paul[2], Hugo Bucher[3], Christian Vérard[2], Thierry Adatte[4], Jeroen E. Sonke[5], Urs Schaltegger[2], Torsten Vennemann[1]

[1]Institute of Earth Surface Dynamics, Géopolis, University of Lausanne, CH-1015 Lausanne, Switzerland

[2]Department of Earth Sciences, Université de Genève, Rue des Maraîchers 13, CH-1205 Genève

[3]Paläontologisches Institut der Universität Zürich, Karl-Schmid-Strasse 4, 8006 Zürich, Switzerland

[4]Institute of Earth Sciences, Géopolis, University of Lausanne, CH-1015 Lausanne, Switzerland

[5]Observatoire Midi-Pyrénées, Géosciences Environnement Toulouse, Université Paul Sabatier Toulouse 3, 14 Avenue Edouard Belin, 31400 Toulouse, France

Corresponding author: Oluwaseun Edward (oluwaseun.edward@unil.ch)

Key Points:

- Mercury concentrations show elevated volcanic fluxes to South China before and after the Permian-Triassic boundary.
- The recorded mercury anomalies are attributed primarily to regional subduction-related arc volcanism, not the Siberian Traps.
- Hg anomalies close to the Permian-Triassic boundary are not a reliable stratigraphic marker for the mass extinction event.

Abstract

Anomalous mercury (Hg) contents recorded near the Permian-Triassic boundary (PTB) are often linked to Siberian Traps Large Igneous Province (STLIP) volcanism and the Permian-Triassic boundary mass extinction (PTBME). However, mounting evidence indicates that the relation between STLIP volcanism and Hg "anomalies" is not straightforward. This study focuses on the timing and provenance of volcanic fluxes around the PTBME in South China. We constrain carbon isotope ($\delta^{13}C$) and Hg concentration and isotope records by utilizing high-precision U-Pb zircon ages from two expanded deep-water marine sections spanning the Late Permian to Early Triassic in the Nanpanjiang Basin. Results reveal two episodes of Hg enrichment. The oldest episode predates the onset of a large negative $\delta^{13}C$ excursion, which is documented to be older than 252.07 ± 0.130 Ma. The second episode occurred between 251.822 ± 0.060 Ma and 251.589 ± 0.062 Ma, coinciding with the nadir of the $\delta^{13}C$ excursion. Volcanic ash geochemistry and Hg isotope compositions suggest that mercury was sourced from subduction-related volcanic arc magmatism in the Tethys region, which peaked between 251.668 ± 0.079 Ma and 251.589 ± 0.052 Ma. These results are compatible with suggestions that regional arc volcanism contributed to the causes of the PTBME in South China and provide evidence that Hg anomalies close to the PTB are not a reliable stratigraphic marker for the PTB extinction event. This study demonstrates that the relations between volcanism, environmental perturbations and mass extinction during the Permian-Triassic transition are better resolved with the aid of high-precision U-Pb zircon ages.

Plain Language Summary

Unusually high mercury contents in sedimentary rock sequences and the mass extinction of organisms during the transition from the Permian–Triassic Period are often linked to Siberian Traps volcanism. However, results from several studies indicate that the relationship between this massive volcanism and mercury peaks in Permian- to Triassic-aged rocks in the South China region is complex. This study combines the geochemical and isotopic records of carbon and mercury from Late Permian to Early Triassic sedimentary rocks, with absolute ages determined from interlayered volcanic ashes, to investigate the presence, timing, and source of volcanic inputs to these rock successions in South China. Results show higher mercury concentrations in two intervals, one before and after the Permian-Triassic boundary. Absolute age results indicate that the mercury peak closest to the Permian-Triassic boundary occurred around 300,000 years after the mass extinction. We attribute the mercury peaks to more local volcanic activity than the far away Siberian Traps and suggest that this regional-scale volcanic activity began shortly before 252 million years ago (Ma) and peaked around 251.6 Ma.

1 Introduction

The Paleozoic – Mesozoic transition (ca. 252 million years ago) was characterized by the largest mass extinction event in the Phanerozoic – the Permian-Triassic boundary mass extinction (PTBME) (Erwin, 1998; Stanley, 2016). This event paved the way for the faunal transition from the Paleozoic evolutionary fauna to the modern fauna (Dal Corso et al., 2022). Furthermore, major perturbations of the global carbon and mercury cycles (expressed as negative carbon (C) isotope excursions and mercury (Hg) concentration spikes, respectively) are documented for sedimentary successions straddling the Permian-Triassic boundary (PTB) in several spatially disparate localities (e.g., Baud et al., 1989; 1996; Grasby et al., 2013; Korte & Kozur, 2010; Sanei et al., 2012; J. Shen et al., 2019; S. Shen et al., 2013; Sial et al., 2020). Causal mechanisms for the extinction are still debated. However, the most popular trigger

suggested by researchers is the temporally overlapping volcanic activity of the Siberian Large Igneous Province (STLIP), based on a temporal overlap between U-Pb ages of STLIP rocks and those of volcanic ash beds in the Meishan Global Stratotype Section and Point (GSSP) (Burgess & Bowring, 2015; Burgess et al., 2017).

The connection between volcanic activity and Hg concentration spikes in sedimentary successions is founded on the understanding that volcanoes are the dominant natural source of Hg to the environment (Pyle & Mather, 2003). As such, LIP volcanism could result in the emission and sequestration of high levels of Hg in the environment. Consequently, mercury "anomalies" – relatively high Hg concentrations or Hg/TOC ratios in a portion of strata within a given sedimentary succession – are used to trace the timing of Large Igneous Province (LIP) magmatism in the geological record (Grasby et al., 2019; Percival et al., 2021; Yager et al., 2021). In the case of the $\delta^{13}C$ record, previous studies have interpreted the negative C isotope excursion associated with the PTB as the result of the intrusion of magma into surrounding organic-rich country rocks (e.g., coal, shale) and petroleum-rich evaporites in the Tunguska Basin, Siberia (Broadley et al., 2018; Payne & Kump, 2007; Svensen et al., 2009). Thus, Hg anomalies and negative $\delta^{13}C$ excursions recorded close to the PTB are usually interpreted in the context of STLIP volcanism and its associated deleterious environmental effects leading to faunal extinction.

However, our understanding of the links between STLIP volcanism, carbon cycle perturbations and mass extinction during the Permian-Triassic (P-T) transition are still complicated by several factors. First, Hg and Hg/TOC content vary significantly near the PTB between different localities and the relative timing of Hg anomalies with regards to the PTBME horizon is inconsistent (e.g., J. Shen et al., 2019; Sial et al., 2020; Wang et al., 2018). In addition, Hg anomalies can also be influenced by factors other than direct volcanic emissions. For instance, Hg anomalies can arise from increased input of Hg remobilized from soils to marine sediments due to increased erosion and continental weathering rates (Them II et al., 2019), as well as enhanced sequestration by sulfides in euxinic depositional environments (J. Shen et al., 2020). In addition, sedimentary Hg records can be distorted by post-depositional weathering, erosion, and thermal alteration (Charbonnier et al., 2020; Chen et al., 2022). Second, the correlation of geochemical records between different localities is fraught with uncertainty because the position of the PTB in many successions remains uncertain (e.g., Johnson et al., 2021; J. Shen et al., 2019; Sial et al., 2020). Also, sedimentary and volcanic successions straddling the Permian and Triassic are often characterized by an unconformity at the PTB (Burgess & Bowring, 2015; Davydov, 2021; Yin et al., 2014), which for South China has been estimated to represent a time gap of about 89 ± 38 kyr for the Permian part (Baresel et al., 2017a). Third, it has become apparent that several paleocontinents, including South China, experienced extensive regional intermediate to felsic volcanism during the P-T transition (Gao et al., 2013; J. Shen et al., 2021; Vajda et al., 2020; Yin et al., 1992; H. Zhang et al., 2021), increasing the potential sources of volcanic Hg input to PTB marine records at these localities. Fourth, absolute time calibration of the eruptive history of the STLIP remains coarse, limiting precise temporal correlations between STLIP magmatism and mass extinction (Dal Corso et al., 2022), although, U-Pb geochronologic evidence suggests that the PTBME may have been limited to only a short period of STLIP magmatism (Burgess et al., 2017). Consequently, considering the complex biogeochemical cycling of Hg, the widespread incompleteness of the PTB rock record (which limits the accuracy of chemostratigraphic and biostratigraphic correlations and the placement of the PTB), and the occurrence of more proximal regional volcanic activity capable

of locally supplying Hg, links between Hg anomalies around the PTB and STLIP magmatism cannot be unequivocally inferred without a thorough assessment of the provenance of the recorded Hg anomalies and their timing relative to the PTBME using precise and accurate geochronology.

Hg isotopes are widely used to trace the sources of Hg anomalies in ancient sedimentary successions, as different transformations during the biogeochemical cycling of Hg can induce mass-dependent (MDF) and/or mass-independent fractionation (MIF) of Hg isotopes (Blum et al., 2014; Thibodeau & Bergquist, 2017). Previous studies have applied Hg isotopes in investigating the source of Hg anomalies and its relationship to the PTBME in P-T successions of South China and elsewhere (Grasby et al., 2017; J. Shen et al., 2021; J. Shen et al., 2019; Wang et al., 2019a; Wang et al., 2018). However, these studies have provided mixed results, with Hg MIF data from nearshore depositional settings reflecting a dominant terrestrial Hg source and those from deeper-water depositional settings being congruent with atmospheric volcanic Hg input (Grasby et al., 2017; Wang et al., 2018). Hence, it has been suggested that the Hg isotope record for these successions mostly reflects their depositional setting (Yager et al., 2021) and that deep-water marine sections, being less vulnerable to terrestrial Hg inputs, may be better suited for investigations of volcanic Hg input sources (Grasby et al., 2017; Thibodeau & Bergquist, 2017; Wang et al., 2018).

The Upper Permian to Lower Triassic of South China is characterized by the widespread occurrence of volcanic ash layers (Gao et al., 2013; He et al., 2014; Yang et al., 2012; Yin et al., 1992), permitting precise and accurate U-Pb zircon geochronological calibrations of P-T successions (e.g., Baresel et al., 2017a, 2017b; Burgess et al., 2014; Lehrmann et al., 2015; S. Shen et al. 2019), as well as providing a means of evaluating the provenance of volcanic products (e.g. zircon) to sedimentary successions in South China (e.g., Jiao et al., 2022; Zhao et al., 2019). However, except for the Shangsi section (with published U-Pb zircon ages, S. Shen et al., 2011), Hg anomalies recorded near the PTB from deep-water marine successions in South China lack U-Pb zircon age calibration. Also, the published U-Pb zircon ages for Shangsi were not obtained with the most recent EARTHTIME spike (S. Shen et al., 2011; Yuan et al., 2019), which makes a direct comparison with ages obtained using this spike problematic at high temporal resolution. To accurately account for spike composition effects on the weighted mean U-Pb age when comparing ages determined using different spikes, the tracer and analytical uncertainty needs to be propagated (i.e., Y uncertainty, see section 2.5, not reported in Shen et al. (2011)). This Y uncertainty propagation results in less-precise ages, inhibiting age comparison at high temporal resolution. In addition to enabling precise geochronology, volcanic ashes provide an archive for the assessment of magmatic sources, as their geochemical compositions reflect those of the source magma (e.g., He et al., 2014; Song et al., 2022; Yang et al., 2012). This study presents, for the first time, a paired $\delta^{13}C$ and Hg (concentration and isotope) record calibrated by precise and accurate U-Pb zircon ages from two sections (Laxian and Potuo) representing deep-water marine depositional environments in the Nanpanjiang Basin, South China. The aim of the study is to assess the occurrence, timing and provenance of volcanic fluxes during the P-T transition in South China.

1.1 Geological Context

The Potuo and Laxian sections (Fig. 1) are situated in the NE-SW trending Pingtang syncline, which in the present-day, is located in the northern part of the Nanpanjiang Basin,

South China (Bagherpour et al. 2020). The Changhsingian (Late Permian) sedimentary succession in Potuo is characterized by thin-bedded siliceous mudstones interbedded with volcanic ash layers: the Talung/Dalong Formation (Bagherpour et al., 2020; Baresel et al. 2017b). The Griesbachian (Induan, Early Triassic) consists of laminated black shales with interbedded concretionary micritic limestones and occasional ash beds representing the Daye/Ziyun Formation (Bagherpour et al., 2020). The Changhsingian to Griesbachian sedimentary succession for Laxian is similar to that of Potuo except that there are no concretionary micritic limestone beds interbedded with the Griesbachian shale units (Bagherpour et al., 2020). The Late Permian to Early Triassic sedimentary sequence in these localities is interpreted to have been deposited as a continuous section in a deep-water basin paleoenvironment, hence without an unconformity between the Talung and Daye formations (Bagherpour et al., 2020; Dai et al., 2019). As such, these sections are ideally suited for our combined geochronologic and geochemical study, having been deposited in troughs within a horst-and-graben paleotopography (Bagherpour et al., 2020). In addition, the presence of volcanic ashes in these sections enables studies of latest Permian to earliest Triassic volcanic fluxes to the Nanpanjiang Basin of South China. Samples spanning the Upper Permian to Lower Triassic used for this study are the same as those analyzed by Bagherpour et al. (2020) and details on the geological setting, lithostratigraphy, biostratigraphy, as well as $\delta^{13}C$ record for these sections are given in that study.

2 Materials and Methods

For this study, measurements of the Hg concentrations (n=70) and isotopic compositions (n=22), total organic carbon (TOC) contents (n=60), major and trace element concentrations for sedimentary rocks and interbedded volcanic ash beds (n=55) were made. These data are complemented by U-Pb zircon geochronology based on single zircon grains from five volcanic ash beds in the two sections (Table S1, supplementary information).

2.1 Stratigraphical correlation of the study sections

Stratigraphical correlation between the two sections studied – Laxian (25.78880°N, 107.29750°E) and Potuo (25.82638°N, 107.24861°E) follows Bagherpour et al. (2020). The PTB is delineated based on the conformable lithostratigraphic boundary between the Talung and Daye formations, which for deep-water sections of the Nanpanjiang Basin, has been shown to be equivalent to the PTB as defined at the Meishan D GSSP based on U-Pb zircon ages (Burgess et al., 2014; Baresel et al., 2017b). The stratigraphical correlation of the Laxian and Potuo sections, which is based on lithostratigraphy (Bagherpour et al. 2020) is congruent with the similarity of the Hg trends for Potuo and Laxian, and is consistent with our new U-Pb zircon ages (see section 3).

2.2 Mercury concentration and isotopic composition

Mercury concentration was measured using a Zeeman R-915F high-frequency atomic absorption spectrometer at the University of Lausanne, Switzerland. Samples (sedimentary rocks, including volcanic ashes) were analyzed in triplicates to ensure analytical precision and the reference material – GSD-11, Chinese alluvium (Hg concentration of 72 ± 9 ppb; Zintwana et al., 2012) was used to monitor accuracy of the measurements (correlation coefficient = 0.99, standard residual deviation = 5 %).

Twenty-two samples (Potuo = 11, Laxian = 11) with sufficiently high Hg concentrations (≥ 9 ppb) were selected for Hg isotopic analysis at the Observatoire Midi-Pyrénées, Toulouse, France. Mercury was preconcentrated using a double-stage tube furnace – acid-trapping protocol as detailed by Sun et al. (2013). Powdered samples were loaded in quartz tubes (pre-cleaned at 550 °C), capped at both ends with quartz wool and heated in a combustion furnace connected to a flow of Hg-free oxygen and set to ramp up from room temperature to 900 °C within 6 hours. Liberated gaseous Hg^0 was then purged into a decomposition oven, held at 1000 °C, using a continuous flow of oxygen. Subsequently, the Hg^0 was collected by oxidation to Hg^{II} in a trapping solution of 40 % (v/v) inverse aqua regia (iAR, $2HNO_3$/1HCl), which was then diluted at the end of the 6 h pre-concentration to 20 % (v/v) iAR and stored at 4 °C in the dark before Hg isotopic measurements (Sun et al., 2013). Two certified reference materials, NIST 1632D (bituminous coal, n=2) and MESS3 (Arctic marine sediment, n=2) were processed along with the samples. Hg isotope compositions were subsequently measured in duplicate over two analytical sessions by cold vapor multi-collector inductively coupled plasma mass spectrometry (CV-MC-ICP-MS) following analytical procedures detailed by Sonke et al., 2010; Sun et al., 2013 and Jiskra et al., 2021. Briefly, the Hg^{II} in the iAR trap solution was reduced to Hg^0 vapor using $SnCl_2$ solution (3 %, w/v, in 1 M HCl) and then analyzed for Hg stable isotopes using an online CETAC HGX-200 cold vapor generator coupled to a Thermo-Scientific Neptune PLUS^{TM} equipped with a 10^{12} Ω resistor on the ^{198}Hg isotope. The MC-ICP-MS instrumental mass bias was corrected by sample-standard bracketing using the NIST 3133 standard at matching standard and sample concentrations (0.71 ppb and 2.1 ppb). Long-term instrumental precision was monitored by repeated analysis of the ETH-Fluka (n = 6) and UM-Almaden (n = 3) Hg standard solutions at Hg concentrations corresponding to the samples (i.e., 0.71 ng/g and 2.1 ng/g). Procedural blanks had an average Hg concentration of ~ 0.01 ng/g (n=3). Mass-dependent fractionation (MDF) of Hg isotopes is reported in small delta notation (δ) as $\delta^{202}Hg$ in permil (‰) relative to the bracketing NIST 3133 standard:

$$\delta^{202}Hg = [((^{202}Hg/^{198}Hg)_{sample}/(^{202}Hg/^{198}Hg)_{NIST3133} - 1) \times 10^3] \quad (1)$$

Mass independent fractionation (MIF) values are denoted using capital delta (Δ) notation and are defined as the difference between the measured values of $\delta^{199}Hg$, $\delta^{200}Hg$, $\delta^{201}Hg$, $\delta^{204}Hg$ and those predicted for MDF with respect to $\delta^{202}Hg$ using the kinetic MDF law as follows:

$$\Delta^{xxx}Hg = \delta^{xxx}Hg - K_{xxx} \times \delta^{202}Hg \quad (2)$$

where xxx refers to Hg isotope masses 199, 200, 201, and 204, and K_{xxx} refers to the constants that are used to calculate values for $\Delta^{xxx}Hg$, which are: 0.2520, 0.5024, 0.7520 and 1.4930 for $\delta^{199}Hg$, $\delta^{200}Hg$, $\delta^{201}Hg$ and $\delta^{204}Hg$ respectively (Blum & Bergquist, 2007). Hg isotopic compositions are reported as the mean of duplicate measurements and analytical uncertainty of isotopic analysis are reported conservatively, as either the 2σ (2 × standard deviation) of the replicate sample measurements or that of the standard with the largest 2σ, whichever was larger. ETH-Fluka and UM-Almaden standard solutions yielded mean values (± 2σ) of -1.48 ± 0.14 ‰, 0.09 ± 0.03 ‰, 0.04 ± 0.03 ‰, 0.04 ± 0.07 ‰; and -0.59 ± 0.09 ‰, -0.03 ± 0.10 ‰, 0.02 ± 0.06 ‰ and -0.05 ± 0.07 ‰ for $\delta^{202}Hg$, $\Delta^{199}Hg$, $\Delta^{200}Hg$, and $\Delta^{201}Hg$ respectively. NIST 1632D and MESS-3 had mean values of -1.93 ± 0.32 ‰, -0.01 ± 0.05 ‰, -0.06 ± 0.08 ‰, -0.06 ± 0.01 ‰; and -2.25 ± 0.02 ‰, 0 ± 0.04 ‰, 0.04 ± 0.03 ‰ and -0.14 ± 0.14 ‰ for $\delta^{202}Hg$, $\Delta^{199}Hg$, $\Delta^{200}Hg$, and $\Delta^{201}Hg$ respectively. These mean values are comparable with reported values for these standard solutions and certified reference materials (Jiskra et al., 2019; Kwon et al., 2015; Sun et al., 2013).

2.3 Organic carbon content

All total organic carbon (TOC) content data for Laxian (n=26) were acquired during the present study. For the Potuo section, 10 data points are from Bagherpour et al. (2020) and an additional 28 samples have been analyzed for this study. Organic matter content and preservation was assessed by Rock-Eval pyrolysis using a Rock Eval^{TM} 6 with the analytical procedures described by Behar et al. (2001). This included measurements of total organic carbon (TOC) content, pyrolysis temperature (T_{max}), hydrogen index (HI) and oxygen index (OI). The standard IFP160000 was used for calibration of the samples and instrumental precision was about 0.1 wt.% for TOC, 10 mg HC/g for HI and 10 mg CO_2/g for OI.

2.4 Major and trace element analysis

Major and trace element concentrations were analyzed by X-ray fluorescence (XRF) spectrometry on glass discs and pressed tablets, respectively, using a PANalytical PW2400 XRF spectrometer at the University of Lausanne, Switzerland. The standard reference materials: JLS-1, JDO-1 and BHVO were used for assessment of analytical accuracy. External reproducibility (1σ) is between 0.5 % and 5 % depending on the element, and detection limit for major elements is ca. 0.01 % and between 1 and 7 ppm for trace elements.

2.5 U-Pb zircon geochronology

In total, nine volcanic ash layers from the Talung (Late Permian) and Daye (Early Triassic) formations at Potuo (POT66T, POT67T, and POT68T) and Laxian (LAX8T, LAX9T, LAX10T, LAX11T, LAX 13T and LAX14T) were processed for U-Pb zircon dating. Of these, seven ash layers yielded sufficient zircon crystals for CA ID-TIMS U-Pb analyses. Zircon U-Pb isotopic compositions were determined by chemical abrasion, isotope dilution, thermal ionization mass spectrometry (CA-ID-TIMS) at the University of Geneva, Switzerland, following the procedure described by Widmann et al. (2019). Zircons were extracted from ash beds by conventional methods (crushing, milling, sieving, magnetic and density separation), including hand-picking of high aspect ratio grains free of visible inclusions. The zircon grains were thermally treated at 900 °C for 48 h to stimulate self-annealing prior to partial dissolution in concentrated hydrofluoric acid (HF_{conc}), to remove structurally damaged domains that may have suffered lead (Pb) loss (see Widmann et al. (2019) for the detailed procedure). The partially dissolved grains were then extracted and washed in 6N HCl in 3 ml Savillex beakers overnight (min. 12 h), at 80 °C. Further cleaning steps involve cycling of 7N HNO_3 and ultra-sonic bathing prior to loading into 200 µl capsules for dissolution in 2 to 3 drops of HF_{conc} for 48 h at 210 °C in pressurized Parr^{TM} vessels. A ^{202}Pb-^{205}Pb-^{233}U-^{235}U tracer solution: ET2535 (EARTHTIME 2535, Condon et al., 2015) was added prior to dissolution, and Pb and U were isolated using ion exchange resin chromatography. Uranium and Pb isotopic compositions were measured on an IsotopX Phoenix TIMS at the University of Geneva. Pb was measured using a dynamic peak jumping routine on a Daly ion counting system, while uranium was measured as UO_2 in static mode using 10^{12} Ω resistor Faraday amplifiers for samples POT66T, POT67T, POT68T, and using ATONA Faraday amplifiers (with a 30 s integration time) for samples LAX8T and LAX10T. The measured isotopic ratios were corrected for interferences of $^{238}U^{18}O^{16}O$ on $^{235}U^{16}O_2$ using a $^{18}O/^{16}O$ composition of 0.00205 based on repeat measurements of the U500 standard. Mass fractionation of U was corrected using a double isotope tracer with a $^{235}U/^{233}U$ of 0.99506 ± 0.005. The Pb blank isotopic composition is $^{206}Pb/^{204}Pb$ = 17.43 ± 0.71 (1σ),

$^{207}Pb/^{204}Pb$ = 14.73 ± 0.38 (1σ) and $^{208}Pb/^{204}Pb$ = 35.58 ± 1.04 (1σ), based on total procedural blank measurements.

U-Pb dates of zircons were calculated using data reduction software Tripoli and ETRedux (Bowring et al., 2011; McLean et al., 2011)), and all uncertainties are reported at the 95 % confidence interval. The interpreted weighted mean age is reported in the format: "weighted mean" ± /X/Y/Z, where X corresponds to analytical uncertainty, Y to analytical + tracer uncertainty and Z to analytical, tracer and decay constant uncertainty (Schoene et al., 2006). All zircon $^{206}Pb/^{238}U$ dates were corrected for ^{230}Th-^{238}U disequilibrium using a Th/U_{magma} of 3.5 ± 1.0. We discuss dates at the precision level of analytical uncertainty (X), since most U-Pb data in the relevant literature were obtained using the same isotope tracer (ET2535) and mode of analysis (ID-TIMS), effectively eliminating inter-lab uncertainty. Repeat analyses of the ET100 solution ($^{206}Pb/^{238}U$ age: 100.173 ± 0.003 Ma; Schaltegger et al., 2021) yielded a value of 100.1678 ± 0.0046 Ma (mean square weighted deviation (MSWD) = 3.2, n = 32/40). One batch comprising 8 ET100 samples was rejected due to an anomalous young average age (this batch is internally consistent). Similarly young, anomalous ET100 ages observed in Schaltegger et al. (2021) were explained by fractionation effects during the sample preparation process. Inclusion of this rejected batch would result in an average ET100 age of 100.1639 ± 0.0039 Ma (MSWD = 3.8, n = 39/40). Excess scatter is indicated by the elevated MSWD value and is commonly observed for the synthetic ET100 solution. This is potentially derived from instrument instability and from the sample preparation process (Schaltegger et al., 2021).

3 Results

Results of all geochemical analyses are given in the supplementary information and presented in figures 2 to 5.

3.1 U-Pb zircon geochronology

A total of 98 zircons from 7 volcanic ash beds were analyzed. Zircon U and Pb data are presented in the supplementary information and interpreted U-Pb dates are illustrated in Fig. 2. For each volcanic ash bed, the U-Pb weighted mean date is interpreted on the following basis: i) not rejecting any analyses that are concordant, ii) the youngest cluster of interpreted concordant zircons consists of ≥ 3 analyses and iii) assuming that all Pb-loss is effectively removed by the chemical abrasion procedure. This data reduction strategy is in line with previous U-Pb ID-TIMS studies concerning volcanic ash beds straddling the Permian-Triassic Boundary and the Early Triassic (e.g., Augland et al., 2019; Baresel et al., 2017b; Burgess et al., 2014; Widmann et al., 2020), making all of these previous ID-TIMS ages directly comparable.

Only in one sample (POT 66T) do we reject one younger, concordant analysis, as it is younger than the statistically significant, slightly older age plateau of 12 analyses (Fig. 2). We assume that this deviation is due to unresolved, residual lead loss not mitigated by the chemical abrasion procedure. Analyses that are older than the youngest, statistically valid, date plateau are considered detrital or due to inherited or antecrystic cores. The principal guideline for the youngest weighted mean age determination is a statistically valid MSWD for the chosen age cluster. Applying this strategy, volcanic ash beds LAX8T, LAX10T, POT66T, POT67T and POT68T have statistically significant $^{206}Pb/^{238}U$ weighted mean ages of 252.07 ± 0.13/0.15/0.31 Ma (Mean Square Weighted Deviation (MSWD) = 1.3, n = 5), 251.822 ± 0.060/0.089/0.28 Ma (MSWD = 1.9, n = 6), 251.589 ± 0.052/0.083/0.28 Ma (MSWD = 1.67, n = 12), 251.668 ± 0.079/0.10/0.29 Ma (MSWD = 1.99, n = 9) and 251.64 ± 0.13/0.15/0.31 Ma (MSWD = 1.5, n =

12), respectively (Fig. 2). Ash beds LAX14T and LAX11T (Table S1) did not satisfy the data reduction criteria outlined above and are thus not interpreted.

3.2 TOC contents and Hg concentrations

TOC content is stratigraphically variable and generally low for Laxian relative to Potuo with a range between < 0.1 – 0.3 wt.% and 0.1 – 2.9 wt.% respectively (Fig. 3). TOC generally shows moderate correlation for Laxian ($r^2 = 0.36$) and Potuo ($r^2 = 0.50$) (Fig. 4). Only 3 samples for Laxian have TOC content above 0.2 wt.%, a suggested threshold for robust Hg/TOC normalization (Grasby et al., 2016). In contrast, only 6 out of 38 samples for Potuo have TOC values < 0.2 wt.%. Therefore, Hg data for Laxian are not normalized to TOC. OI values for Laxian are high, and have a range between 69 and 1386 mg CO_2/g TOC. OI values are between 3 and 334 mg CO_2/g TOC for Potuo, except for volcanic ash samples with values between 64 and 967 mg CO_2/g TOC. HI values are between 19 and 283 mg HC/g TOC and between 17 and 229 mg HC/g TOC for Potuo and Laxian respectively.

Hg concentrations of samples from the Talung Fm. in Potuo are between 2 ppb and 18 ppb and are generally lower than for Laxian, which have a range between 9 ppb and 64 ppb. The main feature of the latest Permian Hg record for Potuo is a minor Hg/TOC excursion (referred to as E1 here) with a peak Hg/TOC value of 70 ppb/wt.%. In the Daye Fm., a significant Hg concentration increase (here labelled as E2) is recorded in the lower part of the successions at both sections. This Hg excursion is simultaneously expressed by the Hg and Hg/TOC records for Potuo (Fig. 3). Peak Hg concentrations within E2 Hg anomaly (Laxian = 251 ppb, Potuo = 203 ppb) are higher than the mean so far reported (62 ppb) for sedimentary rocks (Grasby et al., 2019).

Volcanic ashes from the Talung Fm. at Potuo have Hg concentrations that are at least one order of magnitude higher than for interbedded siliceous mudstones. This difference does not hold in the Daye Fm., where Hg concentration values range between 68 ppb and 165 ppb for volcanic ashes and between 84 ppb and 203 for interbedded rocks within the E2 Hg anomaly interval (Fig. 3b).

3.3 Mercury isotopes

Mass dependent fractionation of Hg isotopes (δ^{202}Hg) shows near-zero to negative values for both sections throughout the studied interval (range: +0.23 ± 0.32 ‰ to -1.75 ± 0.32 ‰; mean = -1.13 ± 1.02 ‰), except for 2 volcanic ash samples from Potuo with more negative values (Fig. 5, POT66T: -2.49 ± 0.32 ‰ and POT67T: -2.29 ± 0.32 ‰).

Hg isotope MIF (Δ^{199}Hg and Δ^{200}Hg) values for both sections are near-zero throughout the studied interval (i.e., 0.1 ‰ > z > -0.1 ‰, where z = sample Hg MIF value), except for sample POT 59, which has a Δ^{199}Hg value of 0.12 ± 0.11 ‰. Mean (± 2σ) Δ^{199}Hg values are 0.02 ± 0.11 ‰ and -0.01 ± 0.11 ‰ for Potuo and Laxian respectively. For Potuo, the mean Δ^{200}Hg value is -0.01 ± 0.10 ‰ and for Laxian, it is 0.00 ± 0.05 ‰. Hence, the Pingtang syncline sections record no measurable mass independent fractionation of Hg isotopes, in contrast to Hg isotope records for deep-water marine sections outside the Nanpanjiang Basin in South China (Fig. 3c).

3.4 Major and Trace Elements

Al_2O_3 concentrations for both sections show similar patterns, having lower values in the Talung Fm. (with a range of 2 to 4 wt.%, except for 1 Potuo sample) relative to the Daye Fm. For Laxian, Al_2O_3 values in the Daye Fm. are 3× higher (range: 15 – 22 wt.%) than those of the Talung Fm. Fe_2O_3 concentrations show a similar trend to Al_2O_3, with lower values in the Talung Fm. (1 to 5 wt.%) relative to the Daye Fm. for both localities. However, unlike Al_2O_3, values in the Daye Fm. for both localities are identical (between 2 and 9 wt.%). Al and Fe (proxied by Al_2O_3 and Fe_2O_3) show little to no correlation with Hg for both Potuo (Al: r^2 =0.02, Fe: r^2 =0.23) and Laxian (Al: r^2 =0.27, Fe: r^2 =0.16). Mo and U are redox-sensitive trace elements used to track redox variations in sedimentary environments (Algeo & Maynard, 2004; Hardisty et al. 2018; Tribovillard et al., 2006). Redox-sensitive trace element concentrations are usually normalized to Al to account for variations that may be unrelated to changes in redox conditions, such as changes in sediment input or authigenic mineral formation (e.g., Algeo & Maynard, 2004; Grasby et al., 2013; Rolison et al., 2017). For Laxian, 73 % of samples analyzed have Mo contents lower than the lower limit of detection (LLD) of the XRF spectrometer (i.e., 1 ppm). Mo/Al values show no stratigraphic trend for either studied locality (Fig. 5e) and have no correlation with Hg contents (Potuo: r^2 = 0.04, Laxian: r^2 = 0.06; Fig. 4D). Laxian samples with measurable Mo (n = 7) have Mo/Al values between 0.1 and 0.6 ppm/wt.%. Mo/Al values for Potuo are slightly higher and range between 0.1 and 1.1 ppm/wt.%, except for sample POT 80 with a value of 5.7 ppm/wt.%. Potuo U/Al values range between 0.2 and 2.3 ppm/wt.%, except for sample POT 63 (U/Al = 4.9 ppm/wt.%). For Laxian, U/Al ranges between 0.2 and 0.8 ppm/wt.%. As with Mo/Al, no correlation is observed between Hg and U/Al (Potuo: r^2 = 0.10, Laxian: r^2 = 0.03; Fig. 4b).

Volcanic ash samples have high LOI (loss on ignition) values between 9 to 14 wt.%, consistent with results from contemporaneous ash layers in South China (He et al., 2014). The ash samples have LOI-corrected mean (± 1σ) concentrations of 58 ± 5 wt.%, 25 ± 2 wt.% and 5 ± 3 wt.% for SiO_2, Al_2O_3 and total alkali (Na_2O+K_2O) respectively (Table S2, supplementary information). To mitigate the chemical effects of secondary alteration of the volcanic ashes, only immobile elements (such as Th, Nb, Ta, Zr, Hf, Ti, Y), known to be unaffected by post-depositional alteration (Portnyagin et al., 2020), are utilized for subsequent chemical classification and tectonic interpretation (Fig. 6). The ashes mainly plot within the fields of rhyodacite/dacite, andesite and trachyandesite on the Nb/Y vs. Zr/Ti diagram (Winchester and Floyd, 1977), separate from STLIP volcanic rocks, except for 1 sample: POT 14T (Fig. 6a). Incompatible trace elements normalized against primitive mantle values (Sun and McDonough, 1989) show that the volcanic ashes are characterized by pronounced negative Nb, Ta and Ti anomalies (Fig. 6d), similar to the trace element pattern for volcanic ashes from other localities in South China (He et al., 2014; Yang et al., 2012).

4 Discussion

4.1 Sedimentary hosts of Hg and interpretation of the Hg anomalies

4.1.1 Hosts of Hg

Hg enrichment in sediments may reflect enhanced Hg sequestration related to increased abundance of its sedimentary host phase(s) or enhanced Hg input fluxes during sediment deposition (Grasby et al., 2019; J. Shen et al., 2020). Due to the high affinity of Hg for organic

matter (OM), Hg concentration is usually normalized to TOC content to account for any OM increases that could have preferentially enhanced Hg sequestration in sediments (e.g., Sanei et al., 2012; Grasby et al., 2017, 2019). However, in samples with low OM content (< 0.2 wt.% TOC), the Hg/TOC ratio is deemed unreliable as the Hg/TOC values become exaggerated, producing false Hg/TOC peaks (Grasby et al., 2019; but see Yager et al., 2021). In addition to TOC variations, Hg sequestration in sedimentary rocks can be influenced by other sedimentary host phases such as clay minerals, iron oxides and sulfides (Charbonnier et al., 2017; J. Shen et al., 2020).

Based on cross plots of Hg vs. TOC, Al, Fe, Mo/Al and U/Al values for both sections, Hg is best correlated to TOC (r^2: Potuo = 0.50 and Laxian = 0.36, Fig. 4c). This correlation suggests that Hg sequestration in the studied sites was partially controlled by organic matter availability and may explain the more efficient sequestration of Hg in the black shales of the Daye Formation relative to the siliceous mudstones of the Talung Formation. Nevertheless, plots of Hg/Al and Hg/Fe ratios for both localities, including Hg/TOC for Potuo (Fig. 3; Fig 5) show similar trends of peak Hg contents in the lower part of the Griesbachian record, suggesting that the Hg anomaly in this interval cannot be explained by TOC variability or clay mineral inputs alone. Furthermore, lithological changes are unlikely to control the Hg concentration spike as increases in Hg concentration do not coincide with the change in lithology in either of the two sections. Moreover, relatively high and low Hg concentrations alike are measured for the Talung and Daye formations where Hg and Hg/TOC anomalies are recorded (Fig. 3; Fig. 8).

4.1.2 Evaluation of Hg preservation

As OM is the dominant host of Hg in the studied successions, the potential impact of post-depositional OM degradation on the Hg record warrants evaluation. Rock-Eval TOC data cross plots (HI, OI, T_{max}) (Fig. 7) are routinely used to evaluate the type and maturity of preserved OM in sedimentary successions (e.g., Charbonnier et al., 2020; Espitalié et al., 1985; Fantasia et al., 2018). The low HI and OI values of many of the samples with enough OM for Rock-Eval data interpretation (i.e., TOC > 0.2 wt.%, Fig. 7a) may indicate diagenetic alteration of marine OM (altered type II) and/or high input of terrestrial OM (type III) (Charbonnier et al., 2020; Fantasia et al., 2018). The range of T_{max} values (400 – 525 °C) suggests that some of the OM in the studied successions are thermally mature and have undergone post-depositional oxidation (Fig. 7b; Espitalié et al., 1985). The thermal maturity of preserved OM in some strata of the studied successions suggests that original Hg contents may have been diagenetically modified (Charbonnier et al., 2020). Consequently, the Hg content measured for strata characterized by thermally mature OM may be a minimum estimate of the original Hg content of these rocks.

Despite the probable partial loss of the original Hg content for some samples, several points argue in favor of the reliability of the general Hg trend documented in the present study. The Changhsingian to Griesbachian Hg trend for both localities is similar despite the vast difference in OM content (Fig. 3). The lack (or loss) of OM is more prevalent in the Laxian succession, yet the background Hg content in this succession is 3× that of Potuo. Also, volcanic ashes mostly have similar Hg content in the Talung and Daye Fm. In contrast, interbedded rocks differ strongly in Hg content between these rock formations (Fig. 3). The much higher Hg content of volcanic ashes despite their higher susceptibility to weathering (e.g., Jiao et al. 2022) and as such, Hg loss, suggests that: i) Hg is reasonably well preserved in these strata, and ii) that the disparity in Hg content between volcanic ashes and interbedded rocks is primary.

Furthermore, both sections record the E2 Hg anomaly, and with a similar excursion magnitude (Fig. 3, Fig. 8). This similarity in the Hg trends and hence, their spatial reproducibility suggests that the primary Hg concentration trends are preserved. In addition, there is no correlation between HI and TOC (Fig. 7c) and little correlation ($r^2 = 0.30$) between HI and Hg values (Fig. 7d), suggesting that OM maturity does not influence Hg trends to any large degree in these successions. Also, the E2 Hg anomaly coincides with the climax of the negative $\delta^{13}C$ excursion at the P-T transition (Fig. 3, Fig. 8), suggesting that the Hg trend is controlled by environmental perturbations (as indicated by the $\delta^{13}C$ excursion), and not diagenetic alteration. Finally, Charbonnier et al. (2020) noted that despite the oxidative weathering of OM observed for weathered rock samples, there were no significant changes in Hg/TOC ratios, suggesting that the Hg/TOC ratio is less susceptible to the effects of post-depositional OM degradation. In the present study, both Hg anomalies reported are present in the Hg/TOC record and more significantly, the main excursion (E2) is present in both the Hg and Hg/TOC record, suggesting that these Hg trends are primary.

4.1.3 Hg isotopes

Hg isotopes are used to trace the source(s) and depositional pathway(s) of Hg to natural environments, as Hg isotope mass-dependent fractionation ($\delta^{202}Hg$) and mass-independent fractionation (MIF, $\Delta^{199}Hg$ and $\Delta^{200}Hg$) compositions vary across Earth surface reservoirs and transport mechanisms (Bergquist & Blum, 2007; Blum et al., 2014; Fu et al., 2021). Here, we focus on Hg isotope MIF, as this occurs via fewer processes compared to MDF (Blum et al., 2014). Also, $\delta^{202}Hg$ values of direct volcanic emissions overlap with those of terrestrial runoff and atmospheric Hg^{II} deposition (Yager et al., 2021), making them less diagnostic than Hg isotope MIF values.

Hg isotope MIF values are considered to be resistant to diagenetic alteration (e.g., Grasby et al. 2017; Thibodeau et al., 2016). This view was recently strengthened by the experimental study of Chen et al. (2022), who documented that high-temperature or high-pressure alteration of rocks does not result in alteration of $\Delta^{199}Hg$ and $\Delta^{200}Hg$ values. $\Delta^{199}Hg$ is commonly used to interpret the sources and pathways of Hg deposition (Thibodeau & Bergquist, 2017; Yager et al., 2021) and recently, $\Delta^{200}Hg$ has been proposed as a complementary tracer of Hg sources to land and oceans (Jiskra et al., 2021). This proposition is because even number-Hg isotope MIF (e.g., $\Delta^{200}Hg$) only occurs via upper atmospheric oxidation-reduction pathways and thus, Hg transformations near Earth's surface yield no measurable even number-Hg isotope MIF (Chen et al., 2012; Fu et al., 2021). Hg from terrestrial biomass usually has negative $\Delta^{199}Hg$ values while oceanic reservoirs (e.g. marine sediments and seawater) are characterized by near-zero to positive $\Delta^{199}Hg$ values (Blum et al., 2014; Yin et al., 2022). Furthermore, Hg released to the atmosphere may undergo MIF via photochemical reactions during its cycling, acquiring positive or negative MIF values (Blum et al, 2014) before long-term burial in marine sediments (Thibodeau et al., 2016). Hg derived from direct volcanic emission is thought to have no measurable MIF (i.e., $\Delta^{199}Hg$, $\Delta^{200}Hg = \sim 0$ ‰, Thibodeau & Bergquist, 2017; Zambardi et al., 2009), consistent with a recent estimate of the $\Delta^{199}Hg$ value of the primitive mantle (0.00 ± 0.10 ‰, Moynier et al., 2021). Therefore, near-zero $\Delta^{199}Hg$ values recorded for rock samples in the geologic record have been interpreted as reflecting unaltered volcanic Hg input to the depositional environment (e.g., Font et al., 2021; Thibodeau et al., 2016; Yager et al., 2021; H. Zhang et al., 2021). Alternatively, near-zero $\Delta^{199}Hg$ values have also been interpreted as

reflecting Hg contributions from a combination of terrestrial and oceanic Hg reservoirs (e.g., J. Shen et al., 2019; 2021; Wang et al., 2019a).

The near-zero and invariant Δ^{199}Hg and Δ^{200}Hg values throughout our studied interval (Fig. 8) are consistent with direct volcanic Hg input from a volcanic center close to the Nanpanjiang Basin, or a mixture of terrestrial and marine Hg sources. Several lines of evidence, however, argue in favor of the former as an explanation for the Hg MIF record of the studied successions. First, the lack of correlation between Hg and Al suggests that Hg sequestration was unrelated to terrestrial input to the Pingtang syncline. As terrestrial input is characterized by negative Hg isotope MIF values (Thibodeau & Bergquist, 2017; Yager et al., 2021; Yin et al., 2022), enhanced clastic input during the Griesbachian (as evidenced by dominantly shale lithology and increase in Al content, Fig. 5) is expected to have resulted in more negative Δ^{199}Hg values. However, Δ^{199}Hg values immediately after the PTB are near-zero to slightly positive for both sites(Fig. 3), suggesting that atmospheric volcanic Hg input was the dominant source of Hg to the Nanpanjiang Basin. Second, the Nanpanjiang Basin was situated close to a volcanic center during the P-T transition. This proximity is evidenced by the occurrence of thicker volcanic ash beds in coeval marine successions in southwest South China (i.e., in the Nanpanjiang Basin) relative to the rest of South China (He et al., 2014; Zhao et al., 2019), the occurrence of coeval acidic-intermediate volcanic and intrusive rocks in southwestern South China and northern Vietnam, as well as copper concentration and isotope excursions linked to felsic "super-eruptions" in South China during the Changhsingian (H. Zhang et al., 2021 and references therein). The paleo-location of the Nanpanjiang Basin may, therefore, also explain the disparity between the Pingtang syncline Hg MIF record and those previously published for other parts of South China (e.g., J. Shen et al., 2021; Wang et al., 2019a; Fig. 3c) (discussed in section 4.4). Third, the Hg isotope MIF values for volcanic ash samples are indistinguishable from those of overlying and underlying strata, suggesting that the source of Hg for volcanic ashes (TOC = ~ 0) and interbedded rocks (TOC = 0 – 3 wt.%) were the same. Consequently, the Hg and Hg/TOC anomalies recorded for both localities are interpreted as dominantly reflective of pulses of elevated atmospheric volcanic Hg input to these deep-water marine depositional sites.

4.2 U-Pb zircon age constraints on the Hg anomaly and C isotope excursion

Although previous works (Grasby et al., 2017; J. Shen et al., 2019; Sial et al., 2020) suggested a coeval global occurrence of Hg anomalies around the PTBME, the majority of sections with defined Hg anomalies around the P-T transition lack high-resolution, high-precision geochronology. Our study attempts to specifically bracket the age of a well-defined Hg anomaly in the Early Triassic via dating of under and overlying ash beds in expanded deep-water marine records. The new U-Pb zircon ages from the Pingtang syncline span the onset of the latest Permian negative δ^{13}C excursion, ca. 252.07 ± 0.130 Ma and brackets a Griesbachian Hg anomaly. The two ash layers analyzed from Laxian straddle the PTB and the U-Pb ages are consistent with the stratigraphy, yielding U-Pb weighted mean ages of 252.07 ± 0.13 Ma (LAX8T, latest Permian) and 251.822 ± 0.060 Ma (LAX10T, Griesbachian) respectively. These U-Pb zircon ages overlap, within analytical error, with the ages of Bed 25 (251.941 ± 0.037 Ma) and Bed 28 (251.880 ± 0.031 Ma) of the very condensed Meishan Global Stratotype Section and Point (GSSP) (Burgess et al., 2014). Thus, the interval between LAX8T and LAX10T includes the PTBME interval at Meishan and also agrees with previous suggestions that the conformable lithological boundary between the Talung/Dalong and Daye/Ziyun formations accurately delineates the PTB in deep-water marine successions in the Nanpanjiang Basin (Bagherpour et

548 al., 2020; Baresel et al., 2017b). Based on lithological comparisons between Potuo and Laxian,
549 the E1 anomaly in Potuo is stratigraphically below LAX 8T (Baghgerpour et al., 2020) and as
550 such, likely predates the mass extinction interval. However, the lack of U-Pb ages in the strata
551 spanning E1 makes quantitative comparisons to LAX 8T uncertain.
552 The overlap between the $^{206}Pb/^{238}U$ weighted mean ages of ash beds POT 66T, 67T and
553 68T suggests the occurrence of several successive volcanic eruptions (within the time covered by
554 these volcanic ash layers) at intervals shorter than the resolving power of our ID-TIMS U-Pb
555 geochronology at the given quality of zircon available for this study. Nevertheless, as these
556 volcanic ash layers from Potuo straddle both the Hg anomaly recorded in the Daye Fm., as well
557 as the coeval nadir of the negative $\delta^{13}C$ excursion (Fig. 8), the age of both the Hg anomaly (E2)
558 and peak C-cycle perturbation during the P-T transition can be determined. The youngest age for
559 both the peak of the E2 Hg anomaly and the nadir of the $\delta^{13}C$ excursion is 251.589 ± 0.052 Ma
560 (POT66T, Fig. 8), while the oldest age estimate is 251.668 ± 0.079 Ma (POT67T). These two
561 ages are identical within the analytical (X) uncertainty, precluding an estimation of the duration
562 of the Hg anomaly. Despite these uncertainties, we can establish with confidence that the post-
563 PTB Hg anomaly peak observed in Potuo is ca. 300 kyr younger (largely outside of analytical
564 uncertainty) than the Meishan PTBME interval (Burgess et al., 2014; Burgess and Bowring,
565 2015), as well as the extinction horizon in Penglaitan (251.939 ± 0.031 Ma; S. Shen et al., 2019).

566 4.2.1 Hg anomalies as a PTBME correlation tool

567 A negative $\delta^{13}C$ excursion at the P-T transition together with a Hg anomaly are common
568 features of many PTB-straddling sedimentary successions (Fig. 9). As such, the peak of the Hg
569 anomaly and/or the nadir of the negative $\delta^{13}C$ excursion associated with the PTB are often
570 considered to be stratigraphic markers for the PTB extinction interval (e.g., Grasby et al., 2017;
571 Sial et al. 2020; J. Shen et al. 2019, 2023; Wignall et al., 1998). Although some sedimentary
572 successions, especially in high latitudes, show Hg excursions coincident with both the negative
573 $\delta^{13}C$ excursion and mass extinction (e.g., Sanei et al., 2012; Grasby et al., 2013), it is apparent
574 that Hg excursions in several other successions straddling the PTB vary in expression, timing,
575 and vertical stratigraphic extent (Fig. 9). Furthermore, local post-depositional processes (e.g.,
576 weathering and burial diagenesis) may lead to the loss of Hg sequestered in rocks, altering the
577 Hg record of these successions (Charbonnier et al., 2020). As such, Hg loss due to post-
578 depositional alteration may partly explain the locally variable expression of Hg anomalies
579 observed for many PTB successions (Fig. 9). However, a thorough assessment of the degree of
580 preservation of rock successions from which P-T transition Hg records have been published
581 would be required to fully explore this possibility. Therefore, the variability of PTB Hg records
582 across different localities questions the reliability of these Hg anomalies for positioning the
583 PTBME and the use of Hg anomalies as a stratigraphic correlation tool.
584 In the case of the Pingtang syncline record, neither Hg excursion (E1 nor E2) temporally
585 corresponds to the extinction interval as calibrated in the Meishan GSSP (Fig. 3; Fig. 8). Also, no
586 Hg anomaly is recorded at the PTBME extinction interval in Laxian (i.e., between LAX 8T and
587 10T, Fig. 3), although the equivalent stratigraphical interval in Potuo is a visibility gap
588 (Bagherpour et al., 2020). As such, the presence of a Hg anomaly there cannot be formally
589 excluded. Nevertheless, our U-Pb zircon ages show that both the nadir of the PTB negative $\delta^{13}C$
590 excursion and the peak of the stratigraphically nearest Hg anomaly to the PTB (E2) are of
591 Griesbachian age (between 251.589 ± 0.052 Ma and 251.668 ± 0.079 Ma). The peak of these
592 excursions therefore, correlate with Bed 33 of the Meishan GSSP (251.583 ± 0.086 Ma, Burgess

et al., 2014), which is much younger than the PTB. Thus, these data provide evidence that although Hg anomalies may coincide with the nadir of the PTB negative $\delta^{13}C$ excursion (Fig. 9), this correspondence cannot be reliably used as a stratigraphic marker for the PTBME in a single section or between different sections (and/or different basins). Similar conclusions were reached for the end-Triassic extinction (ETE) event by Yager et al. (2021), who documented "mismatches in timing" between Triassic-Jurassic boundary Hg anomalies and Central Atlantic Magmatic Province (CAMP) magmatism, which is purported to have triggered the ETE event. Hence, positioning the PTB extinction event by means of and/or correlation based on Hgchemostratigraphy should be treated with extreme caution.

The $\delta^{13}C$ record from Tethyan marine successions (Fig. 9) indicates that the expression of the PTB $\delta^{13}C$ excursion varies between different sections (as previously alluded to by S. Shen et al., 2019). Nevertheless, the PTB (as determined for the individual sections), appears to approximately correspond to the midpoint, not the nadir, of the negative $\delta^{13}C$ excursion in successions not affected by stratigraphic condensation (e.g., Meishan) or a PTB hiatus (Fig. 9). Therefore, it is suggested that in the absence of high-resolution U-Pb zircon age calibration, an approximate correlation of the PTB extinction interval could be achieved using the midpoint of the PTB negative $\delta^{13}C$ excursion. This correlation strategy could be most effective for sections lacking robust biochronology and where the P-T transition $\delta^{13}C$ record is not truncated by a hiatus.

4.3 Does the E2 Hg anomaly of Griesbachian age coincide with a 2nd extinction event?

The onset of the Griesbachian Hg anomaly as recorded from the Laxian section (Fig. 3) postdates LAX 10T, which is dated at 251.822 ± 0.060 Ma. This age coincides, within analytical uncertainty, with that determined for Bed 28 at the Meishan GSSP (251.880 ± 0.031 Ma; Burgess et al., 2014). Because a second step of the PTB mass extinction has been postulated to have occurred within Bed 28 in Meishan (Song et al., 2013), it is pertinent to consider whether the E2 Hg anomaly is associated with this proposed second extinction step.

Conodont biozones around the PTB are usually interval zones (IZs), with the base of each IZ being defined by the first occurrence (FO) of an index species and the top defined by the base of the next overlying IZ. However, this biostratigraphical correlation technique often leads to diachronous correlations because the relative stratigraphic order of FOs of index species is not constant across space, as demonstrated by Brosse et al. (2016) for conodonts around the PTB in South China (see also Ellwood et al., 2017). Reasons for diachronous IZs include ecological control over the distribution of species in time and space, sampling effort, selective preservation, and hiatuses in the sedimentary record (Guex, 1991; Holland & Patzkowsky, 2015; Leu et al., 2022). However, following this approach, the "legal" base Triassic was defined by the FO of *Hindeodus parvus* in the very condensed Meishan section (Yin et al., 2001).

Song et al. (2013) compiled FOs and LOs (last local occurrences) for conodonts and benthic taxa from seven South Chinese PTB sections (including Meishan and Shangsi), which led the authors to propose two extinction steps. The main and older event was placed at the base of the *C. meishanensis* IZ, the antepenultimate IZ below the FO of *H. parvus*. The proposed second extinction step, of lesser magnitude, was found at the base of the *I. isarcica* IZ, which is the third Triassic IZ above the spatially variable FO of *H. parvus.* However, a recent thorough re-investigation of Late Permian conodont IZs in the more expanded Shangsi section (Yuan et al., 2019) led to a revision of the basal Triassic into the *C. meishanensis* IZ. This new placement of the base of the Triassic (Yuan et al. 2019; written comm. 2022) in the *C. meishanensis* IZ in

Shangsi and Meishan has the intrinsic benefit of coinciding with both the main extinction event and the lithostratigraphic boundary between Permian and Triassic rock units, which is marked by a hiatus in outer shelves and shallower depositional settings in South China and elsewhere (Bagherpour et al., 2017; Yin et al., 2014). Close examination of the raw biostratigraphic data (Table S2 of Song et al. 2013) from which a second extinction step was postulated shows no consistent extinction in the relative timing of the different species across the data set. Extinction of a given clade occurs in a single section, or pair of sections at the very best, thus undermining arguments in favor of a second extinction event of global significance. For instance, only the condensed Meishan section displays an apparent second step for benthic foraminifers and bivalves. In Shangsi, no second extinction emerges for any benthic clade around the base of *the I. isarcica* IZ.

Furthermore, the compositing of local extinctions patterns (Song et al. 2013) relies on the implicit assumption of synchronous conodont IZs. However, as the seven sections of this data set cover a very broad range of water depths, ranging from lagoon-shoals to lower slope-basin (Table S1 of Song et al. 2013,), the assumption of synchronous conodont IZs becomes untenable. It is also at variance with the fact that the respective bathymetric distribution of segminate and segminiplanate conodonts, both involved as index species of IZs, is known to be spatially controlled by temperature – i.e., depth of water masses (Joachimski et al., 2012; Leu et al., 2019). Moreover, the general development of a hiatus spanning approximately the entire *C. meishanensis* IZ in shallower depositional settings as clearly established by Yin et al. (2014) automatically excludes any synchronicity of the neighboring IZ when comparing to hiatus-free deep-water sections.

Consequently, because (i) the presence of a stratigraphic hiatus in some sections will inevitably generate a spurious extinction event and (ii) conodont IZs across a depth gradient ranging from lagoonal to basinal depositional settings can hardly be synchronous, there is insufficient biostratigraphic evidence to support a second extinction event in South China. Consequently, it is concluded that the E2 Griesbachian Hg anomaly reported here is not associated with a second extinction pulse in South China.

4.4 Provenance of volcanic Hg input

Our U-Pb geochronological results allow us to place the Pingtang syncline Hg record within the temporal framework of Siberian Traps Large Igneous Province magmatism (Burgess & Bowring, 2015; Burgess et al., 2017), a prominently discussed source of volatiles and toxic elements (such as Hg) during the P-T transition (Black et al., 2012; Broadley et al., 2018; Sibik et al., 2021; Svensen et al., 2018). A maximum duration for intrusive and extrusive magmatic STLIP activity is given by the bracketing ages of 252.27 ± 0.11 Ma (Burgess & Bowring, 2015) to 250.60 ± 0.22 Ma (Augland et al., 2019), the latter from syenitic intrusions with an uncertain relationship to the STLIP. Therefore, STLIP magmatism, being active during the studied interval, is a potential source of volcanic Hg input to South China during the P-T transition.

However, several studies have demonstrated that more proximal regional volcanic activity related to convergent plate tectonism and subduction magmatism occurred during the P-T transition, which led to elevated Hg concentrations and may have contributed to the PTBME in South China (Gao et al., 2013; He et al., 2014; Jiao et al., 2022; H. Zhang et al., 2021; Zhao et al., 2019; Zheng et al., 2020). In addition to Hg/TOC anomalies close to the PTBME horizon, Hg/TOC excursions and corresponding Hg isotope compositions have been documented for the earliest Triassic (Griesbachian) from South China and northern India (Wang et al., 2019a, 2018).

683 Wang et al. (2019a) documented a pair of Hg/TOC anomalies in the latest Permian and earliest
684 Triassic respectively, accompanied by a decreasing trend of Δ^{199}Hg values from the
685 Changhsingian to the Griesbachian. Based on this Δ^{199}Hg trend, they interpreted their
686 Griesbachian Hg/TOC excursion as having resulted from terrestrial Hg input due to elevated
687 Early Triassic continental weathering. Recently, J. Shen et al. (2021) reported several Hg
688 enrichment intervals predating the PTBME (named ME1-ME3), as well as one interval coeval
689 with the PTBME (ME4), from three marine sections in South China. These authors reported the
690 same pattern of decreasing Δ^{199}Hg values from the Changhsingian to Griesbachian. The Hg
691 anomalies preceding the PTBME were interpreted to reflect regional subduction-related
692 volcanism due to their spatial restriction to the Tethys region, the occurrence of numerous
693 volcanic ash layers in Upper Permian rocks across South China, and the geochemical
694 composition of zircons in these ash layers supporting a subduction-zone volcanic arc origin.
695 In contrast with previous studies, the Δ^{199}Hg values in the current study remain near-zero
696 throughout the studied interval, and are slightly positive within the Griesbachian E2 anomaly
697 (Fig. 8). This Δ^{199}Hg trend, despite variations in OM content and detrital flux, is consistent with
698 a constant, dominantly atmospheric volcanic Hg source relatively close to the Nanpanjiang Basin
699 during the studied interval. The disparity between the Hg isotope MIF record of the Pingtang
700 syncline and other deep-water marine records in South China (e.g., Wang et al., 2019a; J. Shen et
701 al., 2021) (Fig. 9), however, suggests that: 1) Hg sequestered in PTB-straddling marine
702 successions in different parts of South China do not have the same source/depositional pathway,
703 and 2) Hg isotope compositions alone may not be sufficient for discriminating between different
704 potential volcanic sources of Hg (e.g., Siberian Traps volcanism or regional arc volcanism) to
705 deep-water depositional sites during the P-T transition in South China.
706 Given that i) Hg excursions in the Pingtang syncline successions are recorded in strata
707 with numerous interbedded volcanic ash layers, ii) the Δ^{199}Hg values of these ashes are
708 indistinguishable from those of interbedded rocks, and iii) the Nanpanjiang Basin was situated
709 close to a volcanic center during the P-T transition, we postulate that the major and trace element
710 geochemical properties of these volcanic ashes can be used to trace the origin of volcanic Hg
711 inputs to these successions. The analyzed volcanic ash beds from Potuo have major and trace
712 element characteristics similar to previously studied volcanic ashes from South China (Fig. 6)
713 (He et al., 2014; Wang et al., 2019b). Their primitive mantle-normalized trace element
714 compositions (Sun & McDonough, 1989) are characterized by depletions in Ta, Nb, Sr and Ti,
715 similar to rocks from subduction settings (Pearce et al., 1995). The ashes show intermediate to
716 acidic chemical compositions, plotting in the field of basaltic andesite, trachy-andesite and
717 rhyolite/dacite (Fig. 6a), and are chemically distinct from volcanic rocks originating from the
718 STLIP (Callegaro et al., 2021; Reichow et al., 2005; Sibik et al., 2015; Sobolev et al., 2009). In
719 addition, a mid-oceanic ridge basalt (MORB)-normalized trace element (Th vs. Nb) discriminant
720 plot (Saccani et al., 2015, 2018) of the volcanic ashes from the Pingtang syncline suggests that
721 they originate from a continental margin volcanic arc tectonic setting (Fig. 6b). Similar
722 conclusions were reached for other volcanic ashes from successions straddling the PTB in South
723 China, in that these ashes have no genetic link to the Siberian Traps, but instead derived from
724 subduction zone arc volcanism in the Tethys region (Gao et al., 2013; He et al., 2014; Jiao et al.,
725 2022; Song et al., 2022; Zhao et al., 2019).
726 Consequently, we conclude that episodic regional arc volcanism associated with
727 convergent plate tectonics in the Tethys region best explains the elevated Hg input to the
728 Nanpanjiang Basin as recorded in the Pingtang syncline during Changhsingian to Griesbachian

times. Furthermore, based on general atmospheric circulation models, previous studies have suggested that the Canadian Arctic was favorably positioned to receive volatiles (including volcanic ash) from the STLIP during the Permian to Triassic because it was situated downwind relative to the location of the STLIP eruptions (Dal Corso et al., 2022; Grasby et al., 2011, 2013). In this scenario, the South China region, being located towards the southeast and several thousands of kilometers away from Siberia, would have been poorly situated to receive volatiles from the STLIP. Nevertheless, STLIP Hg contributions to South China cannot be ruled out. Finally, as noted by J. Shen et al. (2023), volcanic arc magmatism along the eastern margin of the PaleoTethys was especially active during the Permian to Triassic, as inferred from abundant volcanic ash beds in coeval strata, the distribution of volcanic rocks, as well as a number of associated Hg anomalies across the PTB in this region (Fig. 9).

4.5 Hg anomalies, $\delta^{13}C$ excursions and volcanism during the P-T transition

Owing to the paucity of U-Pb zircon ages for deep-water sections from which Hg anomalies have been reported in South China, it is difficult to confidently correlate our recorded Hg anomalies with those reported for other localities in the Tethys region. However, the E1 anomaly recorded from the studied successions together with ME2 and ME3 episodes of J. Shen et al. (2021), indicate that Hg anomalies preceding the PTB extinction are recorded in both shallow and deep-marine settings in South China. In contrast, the E2 Griesbachian Hg anomaly is not recorded from any shallow-water marine section nor deep-water sections in South China, except for deep-water sections in the Nanpanjiang Basin (e.g., Xinmin, Kejiao; Fig. 9). Nevertheless, E2 may be coeval with the Hg anomaly recorded between the *I. staeschei* and *I. isarcica* conodont zones (Wang et al., 2019a), which also coincides with the nadir of the PTB-straddling negative $\delta^{13}C$ excursion in the southwestern Tethys Guryul Ravine section (Fig. 9). However, further work from other marine successions with precise U-Pb zircon ages is required to confirm the spatial extent of the Griesbachian Hg anomaly.

The (stratigraphically variable) coincidence of the nadir of $\delta^{13}C$ excursions with Hg anomalies in the Pingtang syncline and other Tethyan successions (Fig. 9) hints at a common driving factor – volcanism. The global distribution of $\delta^{13}C$ excursions and Hg anomalies close to the PTB in Permian-Triassic successions (Baud et al., 1996; Grasby et al., 2013; Korte & Kozur, 2010; Sanei et al., 2012; J. Shen et al., 2019) argues in favor of a large-scale volcanic degassing episode, such as that of the STLIP, as the ultimate cause of drastic environmental changes of global extent. The onset of the negative $\delta^{13}C$ excursion in the Pingtang syncline starts just before deposition of the ash layer (LAX8T) at 252.07 ± 0.130 Ma (Fig. 8) and is characterized by an initial 2 ‰ decrease in $\delta^{13}C$ values in the upper Changhsingian followed by a further 3 ‰ decrease in the lower Griesbachian. This onset of $\delta^{13}C$ excursion may temporally overlap with the transition from the extrusive Stage 1 to intrusive Stage 2 of STLIP magmatism, proposed to have occurred at about 251.9 Ma (Burgess et al., 2017). Stage 2 STLIP magmatism was characterized by intrusion of dykes and sills into country rocks in the Tunguska Basin (Burgess & Bowring, 2015; Burgess et al., 2017). The intrusions, and subsequent sill complex formation, are proposed to have caused injection of massive amounts of both CO_2 and CH_4 into the atmosphere via contact metamorphism of coal beds, shales and petroleum-bearing evaporites in the Tunguska Basin (Burgess et al., 2017; Svensen et al., 2009, 2018), which collectively are thought to result in a > 5 ‰ negative $\delta^{13}C$ excursion.

However, Davydov (2021) recently questioned the validity of this sill-rock thermal interaction model, pointing out that there is no correlation between coal metamorphism and the

distribution of sills in the Tunguska Basin. This author also argued that the role of contact metamorphism by undifferentiated intrusions, which constitute > 95 % of the Tunguska Basin intrusions, was limited and insignificant to the general coal metamorphism in the Tunguska Basin; and that coal metamorphism in the Tunguska Basin was probably related to regional tectonic deformation instead of magmatism. Furthermore, the role of intrusive STLIP magmatism as a potential driver of the global carbon cycle perturbations and mass extinction during the P-T transition is questioned. This stems from the uncertainty regarding the age of the explosion pipes in the Tunguska Basin (which could have transported CO_2 and other gases such as Hg to the atmosphere), as well as the U-Pb ages of the sill intrusions that violate stratigraphic superposition (Davydov, 2021). Consequently, additional U-Pb zircon geochronologic calibrations of STLIP intrusive rocks are required to resolve these questions.

Pending the resolution of these questions, an additional but not mutually exclusive explanation that could reconcile the coincidence of negative $\delta^{13}C$ excursions and Hg anomalies recorded at a global scale during the P-T transition can be considered. This is that concurrent regional arc volcanism in different palaeocontinents was responsible for both CO_2 and Hg release resulting in the $\delta^{13}C$ excursions and Hg anomalies. In addition to South China, extensive regional arc volcanism during the P-T transition has been documented for many spatially disparate localities. Some of these include: the northern Patagonian Massif, Argentina (Luppo et al., 2018), Antarctica (Nelson & Cottle, 2019), Sydney Basin, Australia (Metcalfe et al., 2015), Karoo Basin, South Africa (Gastaldo et al., 2020), with coeval Hg anomalies also recently documented for the latter two (J. Shen et al., 2023). The suggestion of concurrent regional arc volcanism in several paleocontinents during the P-T transition is congruent with recent suggestions of a Pangean 'ring of fire' (subduction-related volcanism along the convergent Panthalassan margin of Pangea) as an explanation for marine and terrestrial environmental perturbations during the latest Permian (Vajda et al., 2020).

Reasons for a global increase in regional arc volcanism concurrent with STLIP volcanism are still uncertain. Jiao et al. (2022) recently suggested that the ascent of the STLIP mantle plume may have triggered volcanic activity in several subduction zone systems. While the effect of a large mantle plume on global plate tectonics is highly debatable, STLIP volcanism occurred in a context of global increase of accretion and subduction rates from the Permian to Triassic (Vérard et al. 2015a, their Fig. 11a), which has also been linked with Early Triassic sea-level rise (Vérard et al., 2015b, their Fig.17). However, such global increase in subduction rates is likely to occur over tens of millions of years. Hence, increased regional arc volcanism over hundreds of thousands of years between the latest Permian to earliest Triassic may be totally disconnected from global tectonics. Irrespective of the reasons for this global increase in arc volcanism over the P-T transition, our results from the Pingtang syncline suggest that volcanic activity linked to Hg anomalies and C-isotope excursion probably peaked between 251.589 ± 0.052 Ma and 251.668 ± 0.079 Ma in the Nanpanjiang Basin, South China (Fig. 8).

4.6 Implications for the PTBME

While it is generally accepted that STLIP magmatism exerted a major control on the global carbon budget and mercury cycle during the Paleozoic to Mesozoic transition, it is clear that South China was substantially influenced by nearby volcanic centers throughout the Late Permian to Triassic (He et al., 2014; H. Zhang et al., 2021). This is evident from the older and well-known Emeishan LIP (Huang et al., 2022), the occurrence of Permian-Triassic volcanic rocks especially in southwest South China (Gao et al., 2013), the abundant volcanic ash layers

within Permian-Triassic marine sedimentary successions, shown to be genetically distinct from STLIP rocks (Gao et al., 2013; He et al., 2014; Yang et al., 2012), as well as Changhsingian Hg/TOC anomalies restricted to the Tethys region (J. Shen et al., 2021; this study). In addition, regional arc volcanism has been linked to notably decreased carbonate and biogenic silica production, as well as decreased water column oxygenation in South China (J. Shen et al., 2013). The temporal overlap between regional intermediate to felsic volcanism and the basaltic volcanism from the STLIP, thus supports a scenario in which STLIP magmatism and concurrent subduction-related regional arc volcanism in the Tethys region may have acted in concert to generate pernicious environmental conditions for marine and terrestrial faunas in South China during the Late Permian (J. Shen et al., 2013, 2021; S. Shen et al., 2019).

The finding of several sudden increases in mercury concentration that both predate and post-date the PTBME event is significant. This is because these Hg enrichments suggest that elevated volcanic activity, which is thought to have triggered the PTBME in South China, was not restricted only to a short interval e.g., within Stage 2 STLIP magmatism (Burgess et al., 2017), but rather, took place over several thousands of years during the P-T transition. Thus, repeated bursts of regional felsic and intermediate volcanism (and resulting increases in mercury concentration) could have had a cumulative adverse effect on the environment and the species that lived at the time, making them more vulnerable to extinction (J.Shen et al., 2013; 2021; S. Shen et al., 2019). In this scenario, significant environmental stresses resulting from STLIP magmatism would have quite easily pushed faunas in South China "over the edge" to bring about the mass extinction at the Paleozoic-Mesozoic transition.

5 Conclusions

The present study establishes the Hg and $\delta^{13}C$ record of two deep-water marine successions in the Nanpanjiang Basin, South China, spanning the Changhsingian to Griesbachian. U-Pb zircon ages and Hg/TOC ratios indicate elevated volcanic activity before 252.07 ± 0.130 Ma (preceding the PTBME) and during several episodes in the Griesbachian, peaking between 251.589 ± 0.052 Ma and 251.668 ± 0.079 Ma. The latter range in ages is coeval with the nadir of a large negative C isotope excursion, similar in magnitude to the global excursion at the PTB. Based on evidence from the coupled $\delta^{13}C$ and Hg records, major and trace element geochemistry of volcanic ashes, and the U-Pb zircon age constraints, we conclude that the recorded Hg enrichments are primarily sourced from subduction-related arc volcanism in the Tethys region. Consequently, our Hg record together with recent results from South China documenting several episodes of Hg enrichment during the P-T transition, are compatible with previous suggestions that arc volcanism contributed to environmental deterioration and biodiversity decline in South China leading up to the PTBME, which was triggered by STLIP magmatism. Our study provides an absolute timeframe within which Late Permian to Early Triassic Hg and $\delta^{13}C$ records from different deep-water successions (which are less likely to contain stratigraphic gaps) in South China can be calibrated. This precise, radioisotopic timeframe allows for a more in-depth assessment of the relation between volcanism, environmental changes, and the mass extinction event at the P-T transition.

Acknowledgements

This research was supported by a Swiss NSF Sinergia grant (project nr. CRSII5_180253). We thank Olivier Reubi, Edson Ramudzuli and Jérôme Chmeleff for analytical assistance. Special

thanks to Borhan Bagherpour and Marc Leu for providing logs for the study sections, and to members of the Sinergia PaleoC4 team for discussions during the development of this manuscript. The authors also thank Kuang Guodong (Geological survey of Guanxi), Ji Cheng (NIGPAS), Shen Shuzhong (University of Nanjing) for their help related to fieldwork and for scientific discussions.

Conflict of interest

The authors declare no conflict of interest relevant to this study.

Author contributions

Conceptualization & Funding acquisition: Hugo Bucher, Urs Schaltegger, Torsten Vennemann

Formal analysis: Oluwaseun Edward, André N. Paul, Christian Vérard

Investigation: Hugo Bucher, Oluwaseun Edward, André N. Paul, Jeroen Sonke, Thierry Adatte

Resources: Urs Schaltegger, Thierry Adatte, Jeroen Sonke, Torsten Vennemann

Visualization: Oluwaseun Edward, André N. Paul, Christian Vérard

Writing – original draft: Oluwaseun Edward, André N. Paul

Data availability Statement

The dataset associated with the current study is available on the open-source online data repository – Zenodo – at "[*link-to-be-given-upon paper-acceptance*]". Figure 1 was made based on the Panalesis model (Vérard, 2019) using ArcGIS®. Figures 2-8 were made with Matplotlib version 3.5.2 (Caswell et al., 2022), available under the Matplotlib license at https://matplotlib.org, and seaborn version 0.11.2 (Waskom, 2021) available at https://pypi.org/project/seaborn/. All figures were edited using Adobe Illustrator©.

References

Algeo, T.J., Maynard, J.B., 2004. Trace-element behavior and redox facies in core shales of Upper Pennsylvanian Kansas-type cyclothems. *Chemical Geology* 206, 289-318 DOI: https://doi.org/10.1016/j.chemgeo.2003.12.009.

Augland, L. E., Ryabov, V. V., Vernikovsky, V. A., Planke, S., Polozov, A., Callegaro, S., et al. (2019). The main pulse of the Siberian Traps expanded in size and composition. *Scientific reports*, *9*(1), 1-12. https://doi.org/10.1038/s41598-019-54023-2

890 Bagherpour, B., Bucher, H., Baud, A., Brosse, M., Vennemann, T., Martini, R., & Guodun, K.
891 (2017). Onset, development, and cessation of basal Early Triassic microbialites (BETM) in the
892 Nanpanjiang pull-apart Basin, South China Block. *Gondwana Research*, *44*, 178-204.
893 https://doi.org/10.1016/j.gr.2016.11.013
894 Bagherpour, B., Bucher, H., Vennemann, T., Schneebeli-Hermann, E., Yuan, D. X., Leu, M., et
895 al. (2020). Are Late Permian carbon isotope excursions of local or of global significance?
896 *Geological Society of America Bulletin*, *132*(3-4), 521-544. https://doi.org/10.1130/B31996.1
897 Baresel, B., Bucher, H., Bagherpour, B., Brosse, M., Guodun, K., & Schaltegger, U. (2017a).
898 Timing of global regression and microbial bloom linked with the Permian-Triassic boundary
899 mass extinction: implications for driving mechanisms. *Sci Rep*, *7*, 43630.
900 https://doi.org/10.1038/srep43630
901 Baresel, B., Bucher, H., Brosse, M., Cordey, F., Kuang, G. D., & Schaltegger, U. (2017b).
902 Precise age for the Permian-Triassic boundary in South China from high-precision U-Pb
903 geochronology and Bayesian age-depth modeling. *Solid Earth*, *8*(2), 361-378.
904 https://doi.org/10.5194/se-8-361-2017
905 Baud, A., Atudorei, V., & Sharp, Z. (1996). Late Permian and early Triassic evolution of the
906 Northern Indian margin: Carbon isotope and sequence stratigraphy. *Geodinamica acta*, *9*(2-3),
907 57-77. https://doi.org/10.1080/09853111.1996.11105278
908 Baud, A., Magaritz, M., & Holser, W. T. (1989). Permian-Triassic of the Tethys: Carbon isotope
909 studies. *Geologische Rundschau*, *78*, 649-677. https://doi.org/10.1007/BF01776196
910 Behar, F., Beaumont, V., & Penteado, H. L. D. (2001). Rock-Eval 6 technology: Performances
911 and developments. *Oil & Gas Science and Technology-Revue D Ifp Energies Nouvelles*, *56*(2),
912 111-134. https://doi.org/10.2516/ogst:2001013

913 Bergquist, B. A., & Blum, J. D. (2007). Mass-dependent and -independent fractionation of Hg
914 isotopes by photoreduction in aquatic systems. *Science*, *318*(5849), 417-420.
915 https://doi.org/10.1126/science.1148050
916 Black, B. A., Elkins-Tanton, L. T., Rowe, M. C., & Peate, I. U. (2012). Magnitude and
917 consequences of volatile release from the Siberian Traps. *Earth and Planetary Science Letters*,
918 *317*, 363-373. https://doi.org/10.1016/j.epsl.2011.12.001
919 Black, B. A., Neely, R. R., Lamarque, J.-F., Elkins-Tanton, L. T., Kiehl, J. T., Shields, C. A., et
920 al. (2018). Systemic swings in end-Permian climate from Siberian Traps carbon and sulfur
921 outgassing. *Nature Geoscience*, *11*(12), 949-954. https://doi.org/10.1038/s41561-018-0261-y
922 Blum, J. D., & Bergquist, B. A. (2007). Reporting of variations in the natural isotopic
923 composition of mercury. *Anal Bioanal Chem*, *388*(2), 353-359. https://doi.org/10.1007/s00216-
924 007-1236-9
925 Blum, J. D., Sherman, L. S., & Johnson, M. W. (2014). Mercury Isotopes in Earth and
926 Environmental Sciences. *Annual Review of Earth and Planetary Sciences, Vol 42*, *42*, 249-269.
927 https://doi.org/10.1146/annurev-earth-050212-124107
928 Bowring, J. F., McLean, N. M., & Bowring, S. A. (2011). Engineering cyber infrastructure for
929 U-Pb geochronology: Tripoli and U-Pb_Redux. *Geochemistry Geophysics Geosystems*, *12*(6).
930 https://doi.org/10.1029/2010gc003479
931 Broadley, M. W., Barry, P. H., Ballentine, C. J., Taylor, L. A., & Burgess, R. (2018). End-
932 Permian extinction amplified by plume-induced release of recycled lithospheric volatiles. *Nature*
933 *Geoscience*, *11*(9), 682-687. https://doi.org/10.1038/s41561-018-0215-4

Brosse, M., Bucher, H., & Goudemand, N. (2016). Quantitative biochronology of the Permian-Triassic boundary in South China based on conodont unitary associations. *Earth-Science Reviews*, *155*, 153-171. https://doi.org/10.1016/j.earscirev.2016.02.003

Burgess, S. D., Bowring, S., & Shen, S. Z. (2014). High-precision timeline for Earth's most severe extinction. *Proc Natl Acad Sci U S A*, *111*(9), 3316-3321. https://doi.org/10.1073/pnas.1317692111

Burgess, S. D., & Bowring, S. A. (2015). High-precision geochronology confirms voluminous magmatism before, during, and after Earth's most severe extinction. *Science advances*, *1*(7), e1500470. https://doi.org/10.1126/sciadv.1500470

Burgess, S. D., Muirhead, J. D., & Bowring, S. A. (2017). Initial pulse of Siberian Traps sills as the trigger of the end-Permian mass extinction. *Nat Commun*, *8*(1), 164. https://doi.org/10.1038/s41467-017-00083-9

Callegaro, S., Svensen, H. H., Neumann, E. R., Polozov, A., Jerram, D. A., Deegan, F., et al. (2021). Geochemistry of deep Tunguska Basin sills, Siberian Traps: correlations and potential implications for the end-Permian environmental crisis. *Contributions to Mineralogy and Petrology*, *176*(7), 1-30. https://doi.org/10.1007/s00410-021-01807-3

Cao, C., Wang, W., & Jin, Y. (2002). Carbon isotope excursions across the Permian-Triassic boundary in the Meishan section, Zhejiang Province, China. *Chinese Science Bulletin*, *47*(13), 1125-1129. https://doi.org/10.1360/02tb9252

Caswell, T. A., Droettboom, M., Lee, A., Sales De Andrade, E., Hoffmann, T., Klymak, J., et al. (2022). *Matplotlib v3.5.2*. In Zenodo. https://doi.org/10.5281/zenodo.6513224

Charbonnier, G., Adatte, T., Follmi, K. B., & Suan, G. (2020). Effect of Intense Weathering and Postdepositional Degradation of Organic Matter on Hg/TOC Proxy in Organic-rich Sediments

957 and its Implicationsfor Deep-Time Investigations. *Geochemistry Geophysics Geosystems*, *21*(2),
958 e2019GC008707. https://doi.org/10.1029/2019GC008707
959 Charbonnier, G., Morales, C., Duchamp-Alphonse, S., Westermann, S., Adatte, T., & Föllmi, K.
960 B. (2017). Mercury enrichment indicates volcanic triggering of Valanginian environmental
961 change. *Scientific reports*, *7*(1), 1-6. https://doi.org/10.1038/srep40808
962 Chen, D., Ren, D., Deng, C., Tian, Z., & Yin, R. (2022). Mercury loss and isotope fractionation
963 during high-pressure and high-temperature processing of sediments: Implication for the
964 behaviors of mercury during metamorphism. *Geochimica et Cosmochimica Acta*, *334*, 231-240.
965 https://doi.org/10.1016/j.gca.2022.08.010
966 Chen, J., Hintelmann, H., Feng, X., & Dimock, B. (2012). Unusual fractionation of both odd and
967 even mercury isotopes in precipitation from Peterborough, ON, Canada. *Geochimica et*
968 *Cosmochimica Acta*, *90*, 33-46. https://doi.org/10.1016/j.gca.2012.05.005
969 Condon, D. J., Schoene, B., McLean, N. M., Bowring, S. A., & Parrish, R. R. (2015). Metrology
970 and traceability of U-Pb isotope dilution geochronology (EARTHTIME Tracer Calibration Part
971 I). *Geochimica et Cosmochimica Acta*, *164*, 464-480. https://doi.org/10.1016/j.gca.2015.05.026
972 Dai, X., Song, H., Brayard, A., Ware, D., 2019. A new Griesbachian–Dienerian (Induan, Early
973 Triassic) ammonoid fauna from Gujiao, South China. Journal of Paleontology 93, 48-71 DOI:
974 10.1017/jpa.2018.46.
975 Dal Corso, J., Song, H., Callegaro, S., Chu, D., Sun, Y., Hilton, J., et al. (2022). Environmental
976 crises at the Permian–Triassic mass extinction. *Nature Reviews Earth & Environment*, *3*(3), 197-
977 214. https://doi.org/10.1038/s43017-021-00259-4
978 Davydov, V. (2021). Tunguska coals, Siberian sills and the Permian-Triassic extinction. *Earth-*
979 *Science Reviews*, *212*, 103438. https://doi.org/10.1016/j.earscirev.2020.103438

980 Ellwood, B.B., Wardlaw, B.R., Nestell, M.K., Nestell, G.P., Lan, L.T.P., 2017. Identifying
981 globally synchronous Permian–Triassic boundary levels in successions in China and Vietnam
982 using Graphic Correlation. Palaeogeography, Palaeoclimatology, Palaeoecology 485, 561-571
983 DOI: https://doi.org/10.1016/j.palaeo.2017.07.012.
984 Erwin, D.H., 1998. The end and the beginning: recoveries from mass extinctions. Trends in
985 Ecology & Evolution 13, 344-349 DOI: https://doi.org/10.1016/S0169-5347(98)01436-0.
986 Espitalié, J., Deroo, G., Marquis, F., 1985. La pyrolyse Rock-Eval et ses applications. Rev. Inst.
987 Fr. Pétr 40, 563-579 DOI: https://doi.org/10.2516/ogst:1985035.
988 Fantasia, A., Föllmi, K.B., Adatte, T., Bernárdez, E., Spangenberg, J.E., Mattioli, E., 2018. The
989 Toarcian Oceanic Anoxic Event in southwestern Gondwana: an example from the Andean Basin,
990 northern Chile. Journal of the Geological Society 175, 883-902 DOI: 10.1144/jgs2018-008.
991 Font, E., Chen, J., Regelous, M., Regelous, A., Adatte, T., 2021. Volcanic origin of the mercury
992 anomalies at the Cretaceous-Paleogene transition of Bidart, France. Geology 50, 142-146 DOI:
993 10.1130/G49458.1.
994 Fu, X., Jiskra, M., Yang, X., Marusczak, N., Enrico, M., Chmeleff, J., et al. (2021). Mass-
995 Independent Fractionation of Even and Odd Mercury Isotopes during Atmospheric Mercury
996 Redox Reactions. *Environ Sci Technol*, *55*(14), 10164-10174.
997 https://doi.org/10.1021/acs.est.1c02568
998 Gao, Q., Zhang, N., Xia, W., Feng, Q., Chen, Z.-Q., Zheng, J., et al. (2013). Origin of volcanic
999 ash beds across the Permian–Triassic boundary, Daxiakou, South China: petrology and U–Pb
1000 age, trace elements and Hf-isotope composition of zircon. *Chemical Geology*, *360*, 41-53.
1001 https://doi.org/10.1016/j.chemgeo.2013.09.020

1002 Gastaldo, R. A., Kamo, S. L., Neveling, J., Geissman, J. W., Looy, C. V., & Martini, A. M.
1003 (2020). The base of the Lystrosaurus Assemblage Zone, Karoo Basin, predates the end-Permian
1004 marine extinction. *Nature Communications*, *11*(1), 1-8. https://doi.org/10.1038/s41467-020-
1005 15243-7
1006 Grasby, S. E., Sanei, H., & Beauchamp, B. (2011). Catastrophic dispersion of coal fly ash into
1007 oceans during the latest Permian extinction. *Nature Geoscience*, *4*(2), 104-107.
1008 https://doi.org/10.1038/ngeo1069
1009 Grasby, S. E., Sanei, H., Beauchamp, B., & Chen, Z. H. (2013). Mercury deposition through the
1010 Permo-Triassic Biotic Crisis. *Chemical Geology*, *351*, 209-216.
1011 https://doi.org/10.1016/j.chemgeo.2013.05.022
1012 Grasby, S.E., Beauchamp, B., Bond, D.P., Wignall, P.B., Sanei, H., 2016. Mercury anomalies
1013 associated with three extinction events (Capitanian crisis, latest Permian extinction and the
1014 Smithian/Spathian extinction) in NW Pangea. Geological magazine 153, 285-297.
1015 Grasby, S. E., Shen, W. J., Yin, R. S., Gleason, J. D., Blum, J. D., Lepak, R. F., et al. (2017).
1016 Isotopic signatures of mercury contamination in latest Permian oceans. *Geology*, *45*(1), 55-58.
1017 https://doi.org/10.1130/G38487.1
1018 Grasby, S. E., Them, T. R., Chen, Z. H., Yin, R. S., & Ardakani, O. H. (2019). Mercury as a
1019 proxy for volcanic emissions in the geologic record. *Earth-Science Reviews*, *196*, 102880.
1020 https://doi.org/10.1016/j.earscirev.2019.102880
1021 Guex, J. (1991). *Biochronological correlations* (1 ed., Vol. 250). Springer Berlin, Heidelberg.
1022 978-3-540-53937-7
1023 Hardisty, D.S., Lyons, T.W., Riedinger, N., Isson, T.T., Owens, J.D., Aller, R.C., Rye, D.M.,
1024 Planavsky, N.J., Reinhard, C.T., Gill, B.C., 2018. An evaluation of sedimentary molybdenum

and iron as proxies for pore fluid paleoredox conditions. Am J Sci 318, 527-556 DOI: https://doi.org/10.2475/05.2018.04.

He, B., Zhong, Y. T., Xu, Y. G., & Li, X. H. (2014). Triggers of Permo-Triassic boundary mass extinction in South China: The Siberian Traps or Paleo-Tethys ignimbrite flare-up? *Lithos*, *204*, 258-267. https://doi.org/10.1016/j.lithos.2014.05.011

Holland, S. M., & Patzkowsky, M. E. (2015). The stratigraphy of mass extinction. *Palaeontology*, *58*(5), 903-924. https://doi.org/10.1111/pala.12188

Huang, H., Huyskens, M. H., Yin, Q.-Z., Cawood, P. A., Hou, M., Yang, J., et al. (2022). Eruptive tempo of Emeishan large igneous province, southwestern China and northern Vietnam: Relations to biotic crises and paleoclimate changes around the Guadalupian-Lopingian boundary. *Geology*, *50*(9), 1083-1087. https://doi.org/10.1130/G50183.1

Jiao, Y., Zhou, L., Algeo, T. J., Shen, J., Feng, L., Hu, Y., et al. (2022). Zirconium isotopes track volcanic inputs during the Permian-Triassic transition in South China. *Chemical Geology*, *610*, 121074. https://doi.org/10.1016/j.chemgeo.2022.121074

Jiskra, M., Heimburger-Boavida, L. E., Desgranges, M. M., Petrova, M. V., Dufour, A., Ferreira-Araujo, B., et al. (2021). Mercury stable isotopes constrain atmospheric sources to the ocean. *Nature*, *597*(7878), 678-682. https://doi.org/10.1038/s41586-021-03859-8

Jiskra, M., Sonke, J. E., Agnan, Y., Helmig, D., & Obrist, D. (2019). Insights from mercury stable isotopes on terrestrial-atmosphere exchange of Hg(0) in the Arctic tundra. *Biogeosciences*, *16*(20), 4051-4064. https://doi.org/10.5194/bg-16-4051-2019

Joachimski, M. M., Lai, X., Shen, S., Jiang, H., Luo, G., Chen, B., et al. (2012). Climate warming in the latest Permian and the Permian–Triassic mass extinction. *Geology*, *40*(3), 195-198. https://doi.org/10.1130/G32707.1

1048 Johnson, D. L., Present, T. M., Li, M., Shen, Y., & Adkins, J. F. (2021). Carbonate associated
1049 sulfate (CAS) δ34S heterogeneity across the End-Permian Mass Extinction in South China.
1050 *Earth and Planetary Science Letters*, *574*, 117172. https://doi.org/10.1016/j.epsl.2021.117172
1051 Korte, C., & Kozur, H. W. (2010). Carbon-isotope stratigraphy across the Permian-Triassic
1052 boundary: A review. *Journal of Asian Earth Sciences*, *39*(4), 215-235.
1053 https://doi.org/10.1016/j.jseaes.2010.01.005
1054 Kwon, S. Y., Blum, J. D., Nadelhoffer, K. J., Dvonch, J. T., & Tsui, M. T.-K. (2015). Isotopic
1055 study of mercury sources and transfer between a freshwater lake and adjacent forest food web.
1056 *Science of the Total Environment*, *532*, 220-229. https://doi.org/10.1016/j.scitotenv.2015.06.012
1057 Lehrmann, D. J., Stepchinski, L., Altiner, D., Orchard, M. J., Montgomery, P., Enos, P., et al.
1058 (2015). An integrated biostratigraphy (conodonts and foraminifers) and chronostratigraphy
1059 (paleomagnetic reversals, magnetic susceptibility, elemental chemistry, carbon isotopes and
1060 geochronology) for the Permian–Upper Triassic strata of Guandao section, Nanpanjiang Basin,
1061 south China. *Journal of Asian Earth Sciences*, *108*, 117-135.
1062 https://doi.org/10.1016/j.jseaes.2015.04.030
1063 Leu, M., Bucher, H., & Goudemand, N. (2019). Clade-dependent size response of conodonts to
1064 environmental changes during the late Smithian extinction. *Earth-Science Reviews*, *195*, 52-67.
1065 https://doi.org/10.1016/j.earscirev.2018.11.003
1066 Leu, M., Bucher, H., Vennemann, T., Bagherpour, B., Ji, C., Brosse, M., & Goudemand, N.
1067 (2022). A Unitary Association-based conodont biozonation of the Smithian–Spathian boundary
1068 (Early Triassic) and associated biotic crisis from South China. *Swiss Journal of Palaeontology*,
1069 *141*(1), 19. https://doi.org/10.1186/s13358-022-00259-x

1070 Luppo, T., de Luchi, M. G. L., Rapalini, A. E., Dopico, C. I. M., & Fanning, C. M. (2018).
1071 Geochronologic evidence of a large magmatic province in northern Patagonia encompassing the
1072 Permian-Triassic boundary. *Journal of South American Earth Sciences*, *82*, 346-355.
1073 https://doi.org/10.1016/j.jsames.2018.01.003
1074 McLean, N. M., Bowring, J. F., & Bowring, S. A. (2011). An algorithm for U-Pb isotope dilution
1075 data reduction and uncertainty propagation. *Geochemistry Geophysics Geosystems*, *12*(6).
1076 https://doi.org/10.1029/2010GC003478
1077 Metcalfe, I., Crowley, J., Nicoll, R., & Schmitz, M. (2015). High-precision U-Pb CA-TIMS
1078 calibration of Middle Permian to Lower Triassic sequences, mass extinction and extreme
1079 climate-change in eastern Australian Gondwana. *Gondwana Research*, *28*(1), 61-81.
1080 https://doi.org/10.1016/j.gr.2014.09.002
1081 Moynier, F., Jackson, M.G., Zhang, K., Cai, H., Halldórsson, S.A., Pik, R., Day, J.M.D., Chen,
1082 J., 2021. The Mercury Isotopic Composition of Earth's Mantle and the Use of Mass
1083 Independently Fractionated Hg to Test for Recycled Crust. Geophys Res Lett 48,
1084 e2021GL094301 DOI: https://doi.org/10.1029/2021GL094301.
1085 Nelson, D. A., & Cottle, J. M. (2019). Tracking voluminous Permian volcanism of the Choiyoi
1086 Province into central Antarctica. *Lithosphere*, *11*(3), 386-398. https://doi.org/10.1130/l1015.1
1087 Payne, J.L., Kump, L.R., 2007. Evidence for recurrent Early Triassic massive volcanism from
1088 quantitative interpretation of carbon isotope fluctuations. Earth and Planetary Science Letters
1089 256, 264-277 DOI: https://doi.org/10.1016/j.epsl.2007.01.034.
1090 Pearce, J. A. (1982). Trace element characteristics of lavas from destructive plate boundaries. In
1091 R. S. Thorpe (Ed.), *Orogenic andesites and related rocks* (pp. 528-548). John Wiley and Sons.
1092 9780471280347

1093 Pearce, J. A., Baker, P. E., Harvey, P. K., & Luff, I. W. (1995). Geochemical evidence for
1094 subduction fluxes, mantle melting and fractional crystallization beneath the South Sandwich
1095 island arc. *Journal of Petrology*, *36*(4), 1073-1109. https://doi.org/10.1093/petrology/36.4.1073
1096 Portnyagin, M. V., Ponomareva, V. V., Zelenin, E. A., Bazanova, L. I., Pevzner, M. M.,
1097 Plechova, A. A., et al. (2020). TephraKam: geochemical database of glass compositions in tephra
1098 and welded tuffs from the Kamchatka volcanic arc (northwestern Pacific). *Earth System Science*
1099 *Data*, *12*(1), 469-486. https://doi.org/10.5194/essd-12-469-2020
1100 Percival, L.M.E., Bergquist, B.A., Mather, T.A., Sanei, H., 2021. Sedimentary Mercury
1101 Enrichments as a Tracer of Large Igneous Province Volcanism, in: Richard E. Ernst, Alexander
1102 J. Dickson, Bekker, A. (Eds.), Large Igneous Provinces. John Wiley and Sons, Inc., pp. 247-262.
1103 Pyle, D. M., & Mather, T. A. (2003). The importance of volcanic emissions for the global
1104 atmospheric mercury cycle. *Atmospheric Environment*, *37*(36), 5115-5124.
1105 https://doi.org/10.1016/j.atmosenv.2003.07.011
1106 Reichow, M. K., Saunders, A. D., White, R. V., Al'Mukhamedov, A. I., & Medvedev, A. Y.
1107 (2005). Geochemistry and petrogenesis of basalts from the West Siberian Basin: an extension of
1108 the Permo–Triassic Siberian Traps, Russia. *Lithos*, *79*(3), 425-452.
1109 https://doi.org/https://doi.org/10.1016/j.lithos.2004.09.011
1110 Rolison, J.M., Stirling, C.H., Middag, R., Rijkenberg, M.J.A., 2017. Uranium stable isotope
1111 fractionation in the Black Sea: Modern calibration of the 238U/235U paleo-redox proxy.
1112 Geochimica et Cosmochimica Acta 203, 69-88 DOI: https://doi.org/10.1016/j.gca.2016.12.014.
1113 Saccani, E., Delavari, M., Dolati, A., Marroni, M., Pandolfi, L., Chiari, M., & Barbero, E.
1114 (2018). New insights into the geodynamics of Neo-Tethys in the Makran area: Evidence from

age and petrology of ophiolites from the Coloured Mélange Complex (SE Iran). *Gondwana Research*, *62*, 306-327. https://doi.org/10.1016/j.gr.2017.07.013

Saccani, E., Dilek, Y., Marroni, M., & Pandolfi, L. (2015). Continental margin ophiolites of Neotethys: remnants of ancient Ocean–Continent Transition Zone (OCTZ) lithosphere and their geochemistry, mantle sources and melt evolution patterns. *Episodes Journal of International Geoscience*, *38*(4), 230-249. https://doi.org/10.18814/epiiugs/2015/v38i4/82418

Sanei, H., Grasby, S. E., & Beauchamp, B. (2012). Latest Permian mercury anomalies. *Geology*, *40*(1), 63-66. https://doi.org/10.1130/G32596.1

Schaltegger, U., Ovtcharova, M., Gaynor, S. P., Schoene, B., Wotzlaw, J.-F., Davies, J. F., et al. (2021). Long-term repeatability and interlaboratory reproducibility of high-precision ID-TIMS U–Pb geochronology. *Journal of Analytical Atomic Spectrometry*, *36*(7), 1466-1477. https://doi.org/10.1039/D1JA00116G

Schoene, B., Crowley, J. L., Condon, D. J., Schmitz, M. D., & Bowring, S. A. (2006). Reassessing the uranium decay constants for geochronology using ID-TIMS U-Pb data. *Geochimica et Cosmochimica Acta*, *70*(2), 426-445. https://doi.org/10.1016/j.gca.2005.09.007

Shen, J., Algeo, T.J., Hu, Q., Xu, G., Zhou, L., Feng, Q., 2013. Volcanism in South China during the Late Permian and its relationship to marine ecosystem and environmental changes. Global and Planetary Change 105, 121-134 DOI: 10.1016/j.gloplacha.2012.02.011.

Shen, J., Chen, J., Algeo, T. J., Feng, Q., Yu, J., Xu, Y.-G., et al. (2021). Mercury fluxes record regional volcanism in the South China craton prior to the end-Permian mass extinction. *Geology*, *49*(4), 452-456. https://doi.org/10.1130/G48501.1

Shen, J., Chen, J., Algeo, T. J., Yuan, S., Feng, Q., Yu, J., et al. (2019). Evidence for a prolonged Permian-Triassic extinction interval from global marine mercury records. *Nat Commun*, *10*(1), 1563. https://doi.org/10.1038/s41467-019-09620-0

Shen, J., Chen, J., Yu, J., Algeo, T. J., Smith, R. M. H., Botha, J., et al. (2023). Mercury evidence from southern Pangea terrestrial sections for end-Permian global volcanic effects. *Nature Communications*, *14*(1), 6. https://doi.org/10.1038/s41467-022-35272-8

Shen, J., Feng, Q. L., Algeo, T. J., Liu, J. L., Zhou, C. Y., Wei, W., et al. (2020). Sedimentary host phases of mercury (Hg) and implications for use of Hg as a volcanic proxy. *Earth and Planetary Science Letters*, *543*, 116333. https://doi.org/10.1016/j.epsl.2020.116333

Shen, S.-z., Cao, C.-q., Zhang, H., Bowring, S. A., Henderson, C. M., Payne, J. L., et al. (2013). High-resolution δ13Ccarb chemostratigraphy from latest Guadalupian through earliest Triassic in South China and Iran. *Earth and Planetary Science Letters*, *375*, 156-165. https://doi.org/10.1016/j.epsl.2013.05.020

Shen, S.-z., Crowley, J. L., Wang, Y., Bowring, S. A., Erwin, D. H., Sadler, P. M., et al. (2011). Calibrating the end-Permian mass extinction. *Science*, *334*(6061), 1367-1372. https://doi.org/10.1126/science.1213454

Shen, S.Z., Ramezani, J., Chen, J., Cao, C. Q., Erwin, D. H., Zhang, H., et al. (2019). A sudden end-Permian mass extinction in South China. *Geological Society of America Bulletin*, *131*(1-2), 205-223. https://doi.org/10.1130/B31909.1

Sial, A. N., Chen, J. B., Lacerda, L. D., Korte, C., Spangenberg, J. E., Silva-Tamayo, J. C., et al. (2020). Globally enhanced Hg deposition and Hg isotopes in sections straddling the Permian-Triassic boundary: Link to volcanism. *Palaeogeography Palaeoclimatology Palaeoecology*, *540*, 109537. https://doi.org/10.1016/j.palaeo.2019.109537

1159 Sibik, S., Edmonds, M., Maclennan, J., & Svensen, H. (2015). Magmas erupted during the main
1160 pulse of Siberian Traps volcanism were volatile-poor. *Journal of Petrology*, *56*(11), 2089-2116.
1161 https://doi.org/10.1093/petrology/egv064
1162 Sibik, S., Edmonds, M., Villemant, B., Svensen, H. H., Polozov, A. G., & Planke, S. (2021).
1163 Halogen enrichment of Siberian Traps magmas during interaction with evaporites.
1164 https://doi.org/10.3389/feart.2021.741447
1165 Sobolev, A. V., Krivolutskaya, N. A., & Kuzmin, D. V. (2009). Petrology of the parental melts
1166 and mantle sources of Siberian trap magmatism. *Petrology*, *17*(3), 253-286.
1167 https://doi.org/10.1134/S0869591109030047
1168 Song, H., Wignall, P. B., Tong, J., & Yin, H. (2013). Two pulses of extinction during the
1169 Permian–Triassic crisis. *Nature Geoscience*, *6*(1), 52-56. https://doi.org/10.1038/ngeo1649
1170 Song, Q., Hong, H., Algeo, T. J., Fang, Q., Zhao, C., Liu, C., & Xu, Y. (2022). Clay mineralogy
1171 mediated by pH and chemical weathering intensity of Permian–Triassic boundary K-bentonites
1172 at Dongpan (Guangxi, South China). *Chemical Geology*, 121262.
1173 https://doi.org/10.1016/j.chemgeo.2022.121262
1174 Sonke, J. E., Schafer, J., Chmeleff, J., Audry, S., Blanc, G., & Dupre, B. (2010). Sedimentary
1175 mercury stable isotope records of atmospheric and riverine pollution from two major European
1176 heavy metal refineries. *Chemical Geology*, *279*(3-4), 90-100.
1177 https://doi.org/10.1016/j.chemgeo.2010.09.017
1178 Stanley, S.M., 2016. Estimates of the magnitudes of major marine mass extinctions in earth
1179 history. Proceedings of the National Academy of Sciences 113, E6325-E6334 DOI:
1180 10.1073/pnas.1613094113.

1181 Sun, R., Enrico, M., Heimburger, L. E., Scott, C., & Sonke, J. E. (2013). A double-stage tube
1182 furnace--acid-trapping protocol for the pre-concentration of mercury from solid samples for
1183 isotopic analysis. *Anal Bioanal Chem*, *405*(21), 6771-6781. https://doi.org/10.1007/s00216-013-
1184 7152-2
1185 Sun, S.-S., & McDonough, W. F. (1989). Chemical and isotopic systematics of oceanic basalts:
1186 implications for mantle composition and processes. *Geological Society, London, Special*
1187 *Publications*, *42*(1), 313-345. https://doi.org/10.1144/GSL.SP.1989.042.01.1
1188 Svensen, H., Planke, S., Polozov, A. G., Schmidbauer, N., Corfu, F., Podladchikov, Y. Y., &
1189 Jamtveit, B. (2009). Siberian gas venting and the end-Permian environmental crisis. *Earth and*
1190 *Planetary Science Letters*, *277*(3-4), 490-500. https://doi.org/10.1016/j.epsl.2008.11.015
1191 Svensen, H. H., Frolov, S., Akhmanov, G. G., Polozov, A. G., Jerram, D. A., Shiganova, O. V.,
1192 et al. (2018). Sills and gas generation in the Siberian Traps. *Philos Trans A Math Phys Eng Sci*,
1193 *376*(2130), 20170080. https://doi.org/10.1098/rsta.2017.0080
1194 Them II, T., Jagoe, C., Caruthers, A., Gill, B., Grasby, S., Gröcke, D., Yin, R., Owens, J., 2019.
1195 Terrestrial sources as the primary delivery mechanism of mercury to the oceans across the
1196 Toarcian Oceanic Anoxic Event (Early Jurassic). Earth and Planetary Science Letters 507, 62-72
1197 DOI: https://doi.org/10.1016/j.epsl.2018.11.029.
1198 Thibodeau, A. M., & Bergquist, B. A. (2017). Do mercury isotopes record the signature of
1199 massive volcanism in marine sedimentary records? *Geology*, *45*(1), 95-96.
1200 https://doi.org/10.1130/focus012017.1
1201 Thibodeau, A. M., Ritterbush, K., Yager, J. A., West, A. J., Ibarra, Y., Bottjer, D. J., et al.
1202 (2016). Mercury anomalies and the timing of biotic recovery following the end-Triassic mass
1203 extinction. *Nat Commun*, *7*(1), 11147. https://doi.org/10.1038/ncomms11147

1204 Tribovillard, N., Algeo, T.J., Lyons, T., Riboulleau, A., 2006. Trace metals as paleoredox and
1205 paleoproductivity proxies: An update. Chemical Geology 232, 12-32 DOI:
1206 https://doi.org/10.1016/j.chemgeo.2006.02.012.
1207 Vajda, V., McLoughlin, S., Mays, C., Frank, T. D., Fielding, C. R., Tevyaw, A., et al. (2020).
1208 End-Permian (252 Mya) deforestation, wildfires and flooding—an ancient biotic crisis with
1209 lessons for the present. *Earth and Planetary Science Letters*, *529*, 115875.
1210 https://doi.org/10.1016/j.epsl.2019.115875
1211 Vérard, C., Hochard, C., Baumgartner, P. O., Stampfli, G. M., & Liu, M. (2015a). Geodynamic
1212 evolution of the Earth over the Phanerozoic: Plate tectonic activity and palaeoclimatic indicators.
1213 Journal of Palaeogeography, 4(2), 167-188. https://doi.org/10.3724/SP.J.1261.2015.00072
1214 Vérard, C., Hochard, C., Baumgartner, P. O., Stampfli, G. M., & Liu, M. (2015b). 3D
1215 palaeogeographic reconstructions of the Phanerozoic versus sea-level and Sr-ratio variations.
1216 Journal of Palaeogeography, 4(1), 64-84. https://doi.org/10.3724/SP.J.1261.2015.00068
1217 Vérard, C. (2019). Panalesis: towards global synthetic palaeogeographies using integration and
1218 coupling of manifold models. *Geological Magazine*, *156*(2), 320-330.
1219 https://doi.org/10.1017/S0016756817001042
1220 Wang, X., Cawood, P. A., Zhao, H., Zhao, L., Grasby, S. E., Chen, Z.-Q., & Zhang, L. (2019a).
1221 Global mercury cycle during the end-Permian mass extinction and subsequent Early Triassic
1222 recovery. *Earth and Planetary Science Letters*, *513*, 144-155.
1223 https://doi.org/10.1016/j.epsl.2019.02.026
1224 Wang, X., Cawood, P. A., Zhao, L., Chen, Z.-Q., Lyu, Z., & Ma, B. (2019b). Convergent
1225 continental margin volcanic source for ash beds at the Permian-Triassic boundary, South China:

1226 Constraints from trace elements and Hf-isotopes. *Palaeogeography, Palaeoclimatology,*
1227 *Palaeoecology*, *519*, 154-165. https://doi.org/10.1016/j.palaeo.2018.02.011
1228 Wang, X. D., Cawood, P. A., Zhao, H., Zhao, L. S., Grasby, S. E., Chen, Z. Q., et al. (2018).
1229 Mercury anomalies across the end Permian mass extinction in South China from shallow and
1230 deep water depositional environments. *Earth and Planetary Science Letters*, *496*, 159-167.
1231 https://doi.org/10.1016/j.epsl.2018.05.044
1232 Waskom, M. L. (2021). Seaborn: statistical data visualization. *Journal of Open Source Software*,
1233 *6*(60), 3021. https://doi.org/10.21105/joss.03021
1234 Widmann, P., Bucher, H., Leu, M., Vennemann, T., Bagherpour, B., Schneebeli-Hermann, E.,
1235 Goudemand, N., Schaltegger, U., 2020. Dynamics of the largest carbon isotope excursion during
1236 the Early Triassic biotic recovery. *Front Earth Sc-Switz*, 196 DOI:
1237 https://doi.org/10.3389/feart.2020.00196.
1238 Widmann, P., Davies, J. H. F. L., & Schaltegger, U. (2019). Calibrating chemical abrasion: Its
1239 effects on zircon crystal structure, chemical composition and U Pb age. *Chemical Geology*, *511*,
1240 1-10. https://doi.org/10.1016/j.chemgeo.2019.02.026
1241 Wignall, P.B., Morante, R., Newton, R., 1998. The Permo-Triassic transition in Spitsbergen:
1242 δ13Corg chemostratigraphy, Fe and S geochemistry, facies, fauna and trace fossils. *Geological*
1243 *Magazine* 135, 47-62 DOI: 10.1017/S0016756897008121.
1244 Winchester, J. A., & Floyd, P. A. (1977). Geochemical discrimination of different magma series
1245 and their differentiation products using immobile elements. *Chemical Geology*, *20*, 325-343.
1246 https://doi.org/10.1016/0009-2541(77)90057-2
1247 Yager, J. A., West, A. J., Thibodeau, A. M., Corsetti, F. A., Rigo, M., Berelson, W. M., et al.
1248 (2021). Mercury contents and isotope ratios from diverse depositional environments across the

Triassic-Jurassic Boundary: Towards a more robust mercury proxy for large igneous province magmatism. *Earth-Science Reviews*, *223*, 103775. https://doi.org/10.1016/j.earscirev.2021.103775

Yang, J., Cawood, P. A., Du, Y., Huang, H., Huang, H., & Tao, P. (2012). Large Igneous Province and magmatic arc sourced Permian–Triassic volcanogenic sediments in China. *Sedimentary Geology*, *261*, 120-131. https://doi.org/10.1016/j.sedgeo.2012.03.018

Yin, H., Jiang, H., Xia, W., Feng, Q., Zhang, N., & Shen, J. (2014). The end-Permian regression in South China and its implication on mass extinction. *Earth-Science Reviews*, *137*, 19-33. https://doi.org/10.1016/j.earscirev.2013.06.003

Yin, H., Siji, H., Kexing, Z., H.J, H., Fengqing, Y., Meihua, D., Xianmei, B., 1992. The effects of volcanism on the Permo-Triassic mass extinction in South China, in: Dickins, J.M., Sweet, W.C., Zunyi, Y., Hongfu, Y. (Eds.), Permo-Triassic Events in the Eastern Tethys: Stratigraphy Classification and Relations with the Western Tethys. Cambridge University Press, Cambridge, pp. 146-157.

Yin, R., Chen, D., Pan, X., Deng, C., Chen, L., Song, X., Yu, S., Zhu, C., Wei, X., Xu, Y., Feng, X., Blum, J.D., Lehmann, B., 2022. Mantle Hg isotopic heterogeneity and evidence of oceanic Hg recycling into the mantle. Nature Communications 13, 948 DOI: 10.1038/s41467-022-28577-1.

Yin, H., Zhang, K., Tong, J., Yang, Z., & Wu, S. (2001). The global stratotype section and point (GSSP) of the Permian-Triassic boundary. *Episodes*, *24*(2), 102-114. https://doi.org/10.18814/epiiugs/2001/v24i2/004

Yuan, D.-X., Shen, S.-z., Henderson, C. M., Chen, J., Zhang, H., Zheng, Q.-f., & Wu, H. (2019). Integrative timescale for the Lopingian (Late Permian): A review and update from Shangsi,

South China. *Earth-Science Reviews*, *188*, 190-209. https://doi.org/10.1016/j.earscirev.2018.11.002

Zambardi, T., Sonke, J. E., Toutain, J. P., Sortino, F., & Shinohara, H. (2009). Mercury emissions and stable isotopic compositions at Vulcano Island (Italy). *Earth and Planetary Science Letters*, *277*(1-2), 236-243. https://doi.org/10.1016/j.epsl.2008.10.023

Zhang, G. J., Zhang, X. L., & Shen, Y. N. (2021). Quantitative constraints on carbon cycling and temporal changes in episodic euxinia during the end-Permian mass extinction in South China. *Chemical Geology*, *562*, 120036. https://doi.org/10.1016/j.chemgeo.2020.120036

Zhang, H., Zhang, F., Chen, J. B., Erwin, D. H., Syverson, D. D., Ni, P., et al. (2021). Felsic volcanism as a factor driving the end-Permian mass extinction. *Sci Adv*, *7*(47), eabh1390. https://doi.org/10.1126/sciadv.abh1390

Zhao, T. Y., Algeo, T. J., Feng, Q. L., Zi, J. W., & Xu, G. Z. (2019). Tracing the provenance of volcanic ash in Permian-Triassic boundary strata, South China: Constraints from inherited and syn-depositional magmatic zircons. *Palaeogeography Palaeoclimatology Palaeoecology*, *516*, 190-202. https://doi.org/10.1016/j.palaeo.2018.12.002

Zheng, B. S., Mou, C. L., Zhou, R. J., Wang, X. P., Xiao, Z. H., & Chen, Y. (2020). Nature and origin of the volcanic ash beds near the Permian-Triassic boundary in South China: new data and their geological implications. *Geological Magazine*, *157*(4), 677-689. https://doi.org/10.1017/S001675681900133x

Zintwana, M. P., Cawthorn, R. G., Ashwal, L. D., Roelofse, F., & Cronwright, H. (2012). Mercury in the Bushveld Complex, South Africa, and the Skaergaard Intrusion, Greenland. *Chemical Geology*, *320*, 147-155. https://doi.org/10.1016/j.chemgeo.2012.06.001

Figure Captions

Figure 1. Maps showing the location of the studied successions, as well as other marine successions in the Tethys region from which Permian-Triassic (P-T) transition mercury records have been published. a) Global paleogeographic map at the P-T transition after the Panalesis model (Vérard, 2019). Locality marked '10' represents the paleo-location of Guryul Ravine, northern India. b) Map showing the present-day location of the studied sections (red circles) and other deep-water marine sections in South China (yellow circles); white circles show the main cities. The sections are represented by numbers as follows: 1 – Meishan, 2 – Majiashan, 3 – Daxiakou, 4 – Xiakou. 5 – Shangsi, 6 – Laxian, 7 – Potuo, 8 – Xinmin, 9 – Kejiao. c**)** Detailed map of the South China area (orthogonal projection) with the paleo-location of the discussed sections.

Figure 2. Single-grain zircon analyses and $^{206}Pb/^{238}U$ weighted mean dates for volcanic ash beds from Potuo and Laxian. Bars represent single grain zircon U-Pb dates and their uncertainty. Transparent bars are rejected for interpretation (Pb-loss, inheritance, antecrystic).

Figure 3. Carbon isotope values, Hg concentrations, Hg/TOC ratios, TOC contents and $\Delta^{199}Hg$ values from a) Laxian, b) Potuo. The gap between the Talung and Daye formations in the Potuo stratigraphic log is an observation gap due to coverage by alluvium (Bagherpour et al., 2020). Black dashed lines represent the 0.2 wt.% TOC limit for Hg/TOC normalization (Grasby et al., 2019) and green dashed lines represent background $\delta^{13}C_{org}$ values (-27 ‰). Box and whisker plots of c) $\Delta^{199}Hg$ values and d) $\Delta^{200}Hg$ values for Potuo and Laxian compared to those previously documented for other deep-water marine sections in South China. Grey shaded rectangle (in a, b) and red dashed lines (in c, d) represent the interval of no measurable Hg isotope mass independent fractionation (MIF, 0 ± 0.05 ‰). Data sources are as follows: Majiashan - Wang et al.(2019a), Daxiakou - Wang et al. (2018), Xiakou - J. Shen et al. (2019), Shangsi - J. Shen et al. (2021).

Figure 4. Scatter plot showing the relationship between Hg and a) Al, b) U/Al, c) TOC, d) Mo/Al and e) Fe in the Pingtang syncline sections. Black dashed line represents 0.2 wt.% TOC limit (Grasby et al., 2016). Volcanic ash samples are not included in the calculation of the correlation coefficient squared (r^2).

Figure 5. Composite plot of Hg/element ratios and Hg isotope mass dependent fractionation values for Potuo and Laxian. a) Al, b) Hg/Al, c) Hg/Fe, d) Hg/TOC, e) Mo/Al, f) U/Al, g) $\delta^{202}Hg$. Symbols of lithological log are identical to those of Fig. 3. The composite section is based on lithological comparison of the Potuo and Laxian sections (Bagherpour et al., 2020) and assumes similar sedimentation rates for both sections. Note that the Potuo and Laxian sections are only 6.4 km apart and both belong to the Pingtang syncline of the Nanpajiang Basin, recording laterally continuous basinal facies belonging to the Talung Fm. and Daye Fm. (Bagherpour et al., 2020).

Figure 6: Major and trace element geochemistry results for volcanic ash samples from the Pingtang syncline. A) Zr/Ti vs Nb/Y classification diagram (Winchester & Floyd, 1977) for volcanic ashes from South China plotted along with volcanic rocks from the Siberian Traps Large Igneous Province (STLIP) b) N-MORB-normalized Th vs. Nb discriminant plot, with tectonic setting interpretation after Saccani et al. (2015, 2018) for volcanic ashes from South

China, together with data from dolerite sills, dykes and basalts from the STLIP (Tunguska Basin) plotted for comparison. N-MORB: normal-type mid-oceanic ridge basalt. C) Ti vs Zr classification diagram after Pearce (1982). The field illustrating typical Siberian Traps volcanic rock compositions is after He et al. (2014). D) Primitive mantle-normalized spider diagram for Changhsingian and Griesbachian volcanic ashes from Potuo and other localities (Meishan, Chaotian, Jianshi, Rencunping, Shangsi and Dongpan) in South China. Data for South China localities other than Potuo are from He et al. (2014), Song et al. (2022) and Wang et al. (2019b). Normalization values for N-MORB and primitive mantle are from Sun & McDonough (1989). Data for volcanic rocks from the STLIP are from several sources as follows: basalt flows, dolerite sills, dykes: Sibik et al. (2015); Callegaro et al. (2021); magnesian rocks, melt inclusions: Sobolev et al. (2009); West Siberia Basin (WSB) basalts: Reichow et al. (2005). WSB: West Siberia Basin, SC: South China.

Figure 7. Cross plots of Rock-Eval TOC data for samples with TOC > 0.2 wt.% to assess the type and quality of preserved organic matter in Potuo and Laxian (modified after Charbonnier et al., 2020). A) HI vs OI, b) HI vs T_{max}, c) HI vs TOC, d) Hg vs Hg.

Figure 8. Composite profiles for a) $\delta^{13}C$, b) Hg concentration, c) Hg/TOC ratios, d) $\Delta^{199}Hg$, e) $\Delta^{200}Hg$ records from the Potuo and Laxian sections. $\delta^{13}C$ values are from Bagherpour et al. (2020). The horizontal gray band marks the interval of Hg concentration spike (E2) and nadir of the negative $\delta^{13}C$ excursion and the vertical pink bands depict near-zero Hg isotope MIF (0 ± 0.05 ‰, Thibodeau et al., 2016). The dashed green line represents the conformable Talung-Daye formational boundary and the PTB. The Siberian Traps magmatism timeline is after Burgess et al. (2017) and the color gradient between the stages depicts the uncertainty in the timing of the transition between different stages. The PTB on the composite log is defined from the Laxian section as this interval at Potuo is covered by recent alluvial deposits (Bagherpour et al., 2020). U-Pb zircon ages for the PTB (in green) are from (a) Burgess et al. (2014) and (b) Baresel et al. (2017b). FO – first occurrence.

Figure 9. Compilation of carbon (organic and carbonate) isotope, mercury (Hg) concentration, Hg/TOC and Hg isotope ($\Delta^{199}Hg$) records for marine depositional environments in the Tethys region: South China and northern India. Hg/TOC ratios are shown only for localities and stratigraphic intervals where TOC content is > 0.2 wt.%. a)Shangsi, b) Xiakou, c) Majiashan, d) Daxiakou, e)Xinmin, f) Kejiao, g) Pingtang syncline (composite of the Potuo and Laxian sections), h) Meishan. U-Pb zircon ages are from Burgess et al. (2014), i) Guryul Ravine, northern India. The different profiles are correlated using the Permian-Triassic boundary as placed by the authors of the original data sources. Data sources are as follows: Meishan: Cao et al. (2002); Grasby et al. (2017) and J. Shen et al. (2019); Guryul Ravine and Majiashan: Wang et al. (2019a); Shangsi: J. Shen et al. (2021); Xiakou: J. Shen et al. (2019); G.J. Zhang et al. (2021); Xinmin, Kejiao: J. Shen et al. (2019); Daxiakou: Wang et al. (2018); Pingtang syncline (Potuo, Laxian): this study. U-Pb zircon age for the Permian-Triassic boundary (in green) is from Burgess et al. (2014). Abbreviations: Gries.: Griesbachian; *: *Hindeodus latidentatus; C.m: Clarkina meishanensis*; **: *Hindeodus parvus; H.p: Hindeodus praeparvus; I.st.: Isarcicella staeschei; Nc.kry.: Neoclarkina krystyni; C.y..: Clarkina yini; C.tay.: Clarkina taylorae.*

Figure 1.

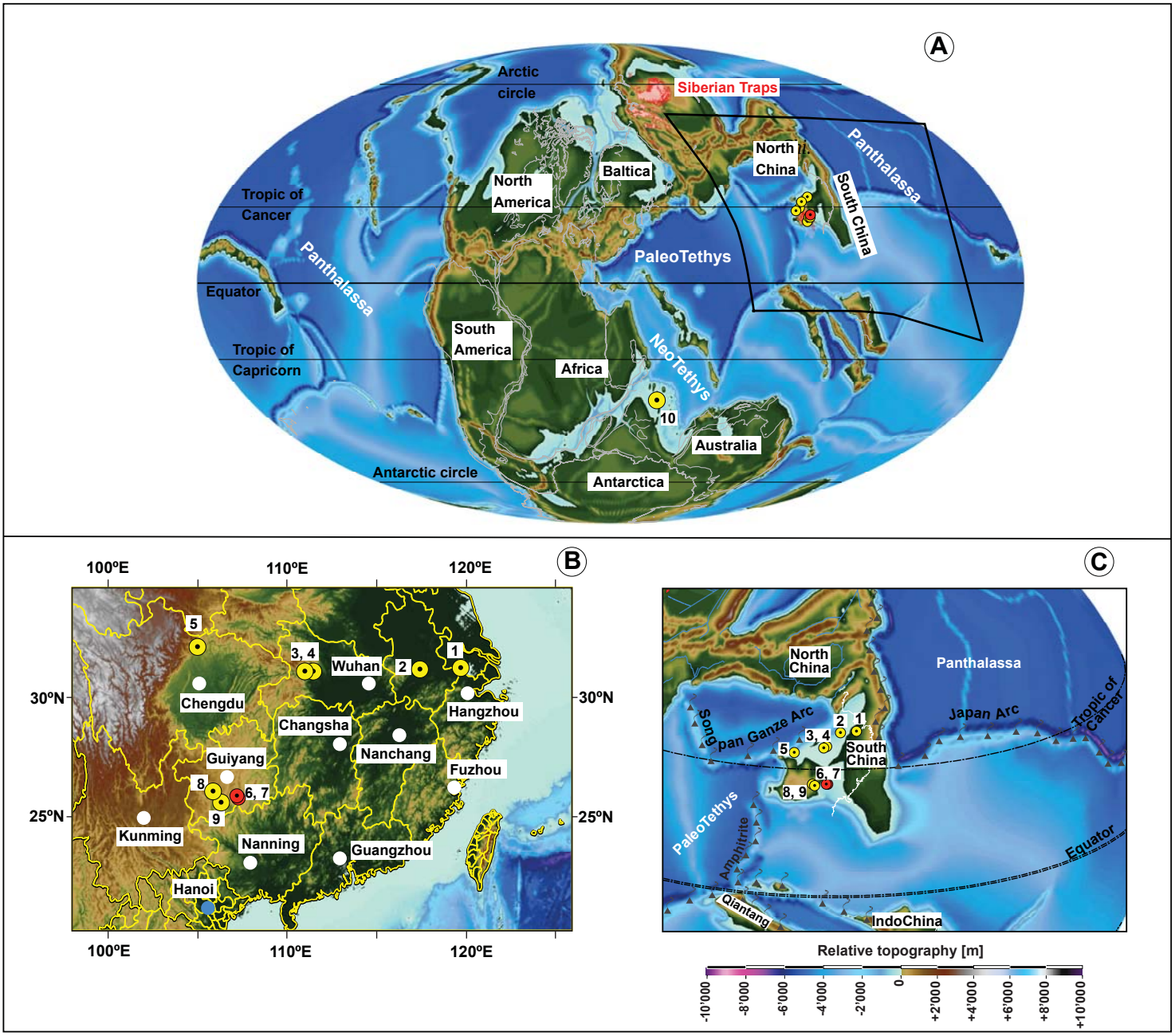
A
Arctic circle
Siberian Traps
Panthalassa
North China
Baltica
North America
Tropic of Cancer
South China
Panthalassa
PaleoTethys
Equator
South America
NeoTethys
Tropic of Capricorn
Africa
10
Australia
Antarctic circle
Antarctica
B
100ºE
110ºE
120ºE
30ºN
25ºN
5
3, 4
Wuhan
2
1
Chengdu
Hangzhou
Changsha
Nanchang
Guiyang
Fuzhou
8
6, 7
9
Kunming
Nanning
Guangzhou
Hanoi
C
North China
Panthalassa
Songpan Ganze Arc
Japan Arc
Tropic of Cancer
2
1
3, 4
5
South China
6, 7
8, 9
PaleoTethys
Amphitrite
Equator
Qiantang
IndoChina
Relative topography [m]
-10'000
-8'000
-6'000
-4'000
-2'000
0
+2'000
+4'000
+6'000
+8'000
+10'000

Figure 2.

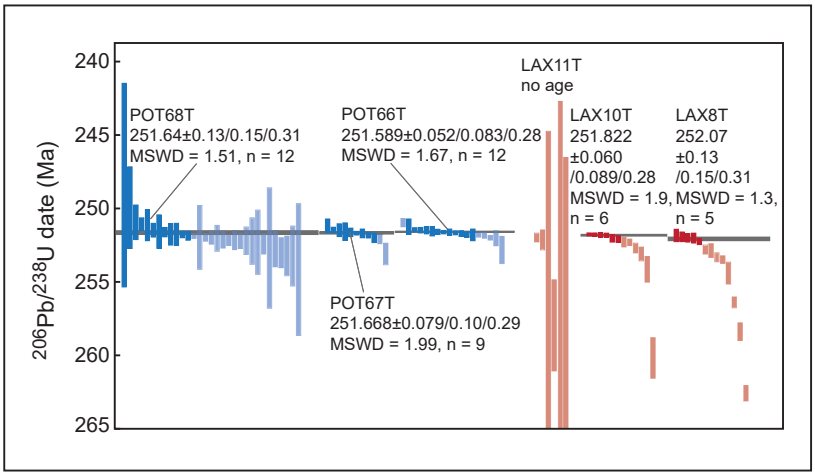
240
245
250
255
260
265
$^{206}Pb/^{238}U$ date (Ma)
POT68T
251.64±0.13/0.15/0.31
MSWD = 1.51, n = 12
POT66T
251.589±0.052/0.083/0.28
MSWD = 1.67, n = 12
POT67T
251.668±0.079/0.10/0.29
MSWD = 1.99, n = 9
LAX11T
no age
LAX10T
251.822
±0.060
/0.089/0.28
MSWD = 1.9,
n = 6
LAX8T
252.07
±0.13
/0.15/0.31
MSWD = 1.3,
n = 5

Figure 3.

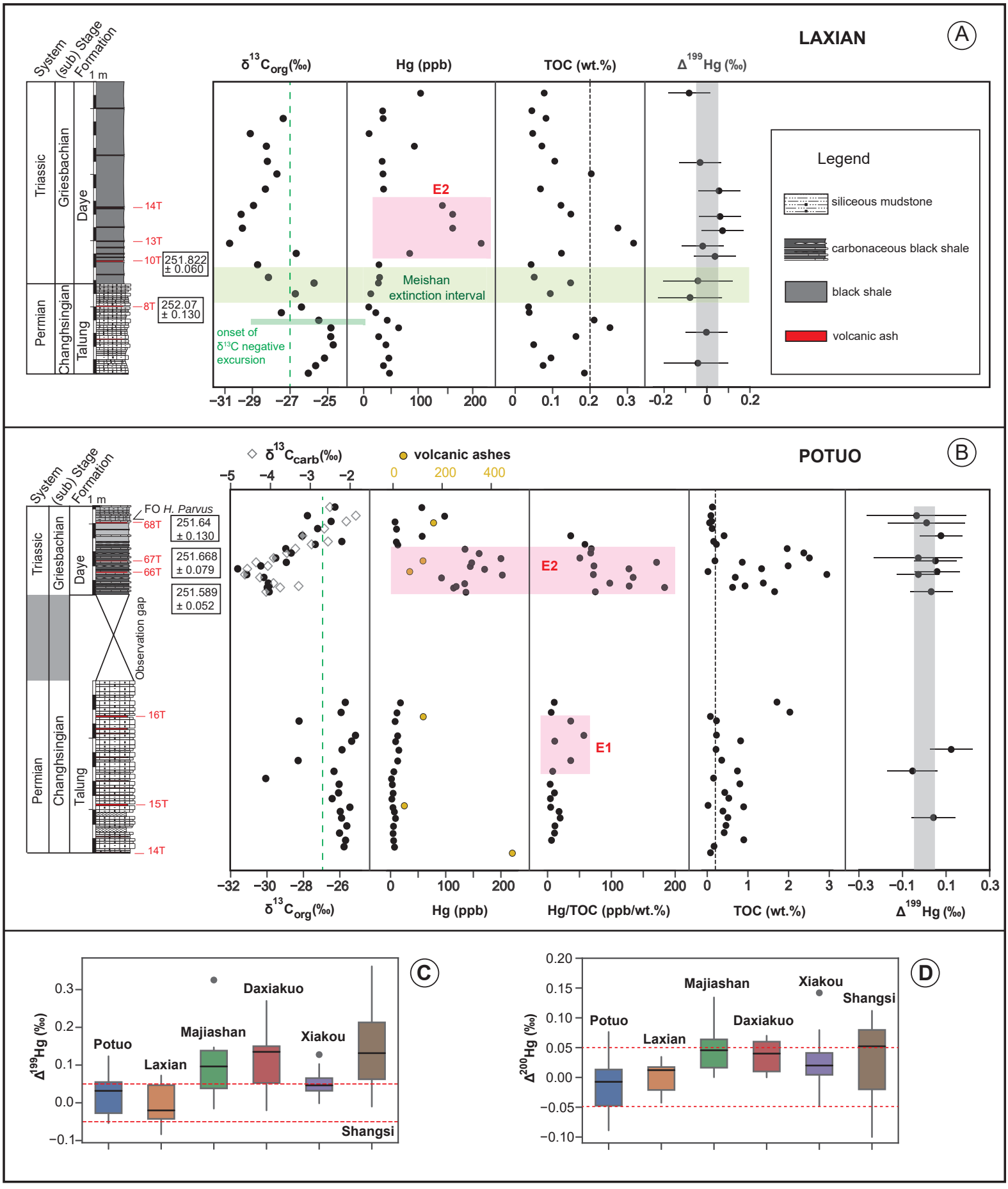
LAXIAN
A
System
(sub) Stage
Formation
1 m
Triassic
Griesbachian
Daye
Permian
Changhsingian
Talung
14T
13T
10T
251.822
± 0.060
8T
252.07
± 0.130
δ13Corg(‰)
Hg (ppb)
TOC (wt.%)
Δ199Hg (‰)
E2
Meishan
extinction interval
onset of
δ13C negative
excursion
Legend
siliceous mudstone
carbonaceous black shale
black shale
volcanic ash
−31 −29 −27 −25
0 100 200
0 0.1 0.2 0.3
−0.2 0 0.2
POTUO
B
δ13Ccarb(‰)
volcanic ashes
−5 −4 −3 −2
0 200 400
FO H. Parvus
68T
251.64
± 0.130
67T
66T
251.668
± 0.079
251.589
± 0.052
Observation gap
16T
15T
14T
E2
E1
−32 −30 −28 −26
0 100 200
0 100 200
0 1 2 3
−0.3 −0.1 0.1 0.3
δ13Corg(‰)
Hg (ppb)
Hg/TOC (ppb/wt.%)
TOC (wt.%)
Δ199Hg (‰)
C
Δ199Hg (‰)
0.3
0.2
0.1
0.0
−0.1
Potuo
Laxian
Majiashan
Daxiakuo
Xiakou
Shangsi
D
Δ200Hg (‰)
0.20
0.15
0.10
0.05
0.00
−0.05
−0.10
Potuo
Laxian
Majiashan
Daxiakuo
Xiakou
Shangsi

Figure 4.

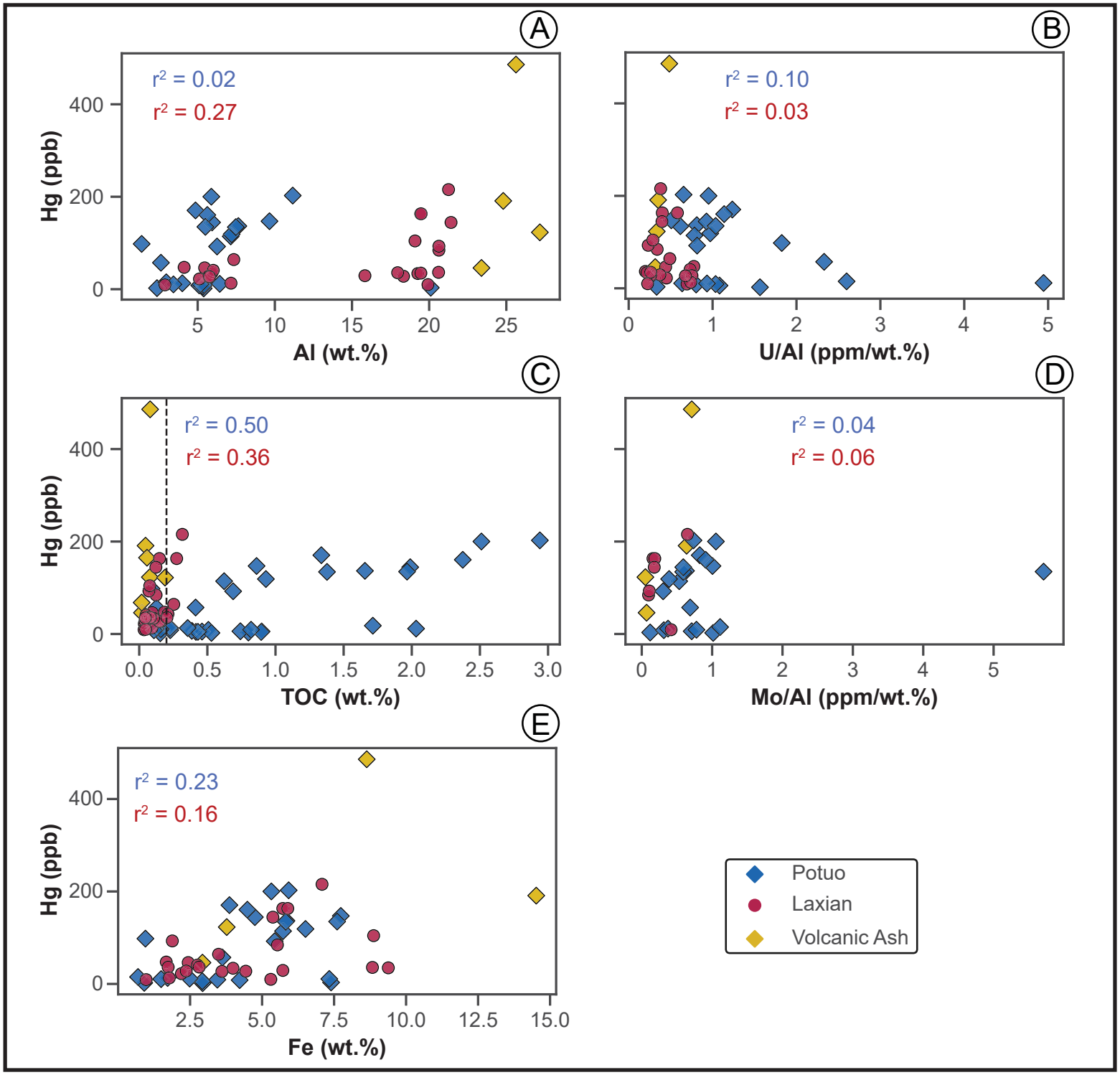
A
r² = 0.02
r² = 0.27
Hg (ppb)
400
200
0
5
10
15
20
25
Al (wt.%)
B
r² = 0.10
r² = 0.03
0
1
2
3
4
5
U/Al (ppm/wt.%)
C
r² = 0.50
r² = 0.36
Hg (ppb)
400
200
0
0.0
0.5
1.0
1.5
2.0
2.5
3.0
TOC (wt.%)
D
r² = 0.04
r² = 0.06
0
1
2
3
4
5
Mo/Al (ppm/wt.%)
E
r² = 0.23
r² = 0.16
Hg (ppb)
400
200
0
2.5
5.0
7.5
10.0
12.5
15.0
Fe (wt.%)
Potuo
Laxian
Volcanic Ash

Figure 5.

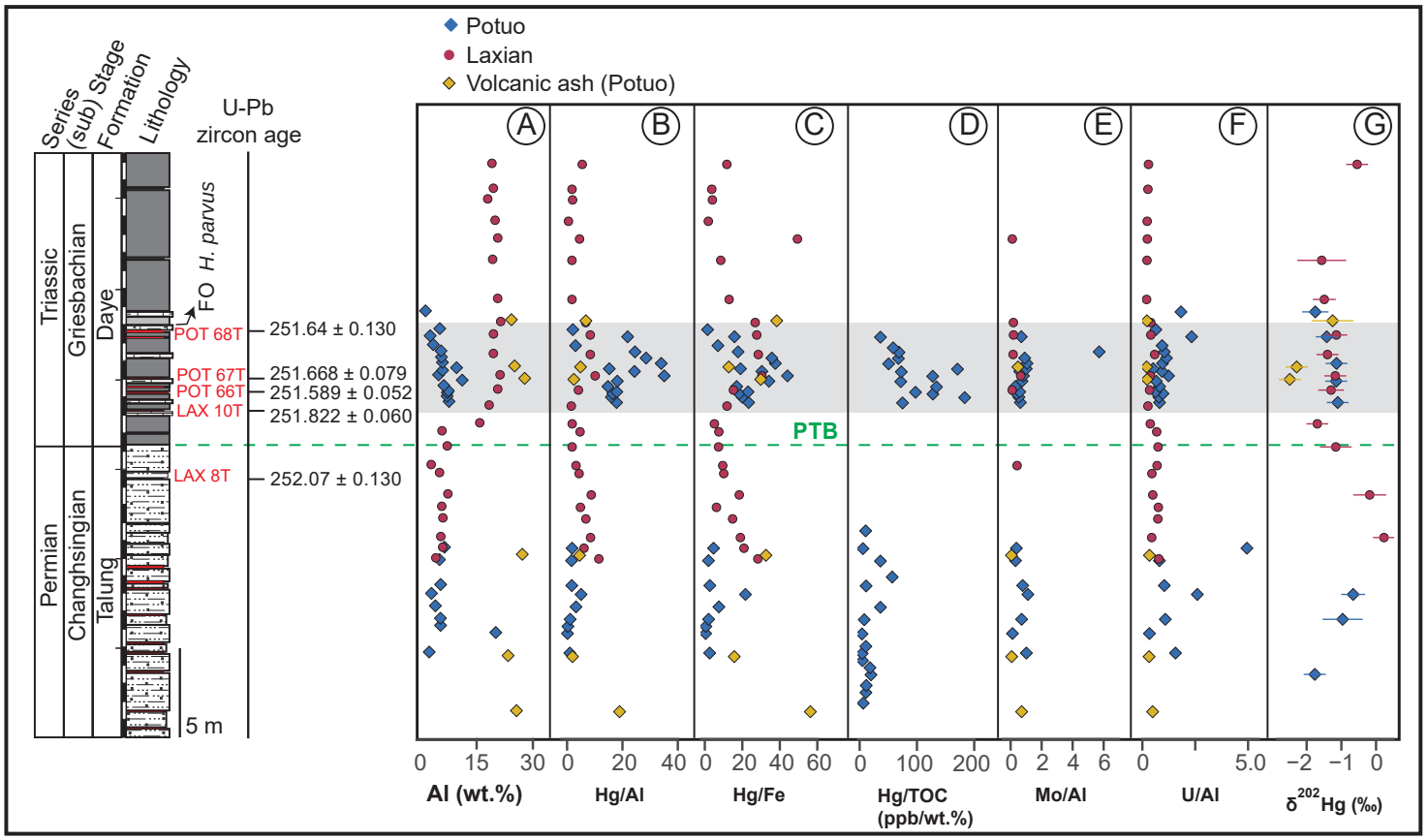
Potuo
Laxian
Volcanic ash (Potuo)
Series
(sub) Stage
Formation
Lithology
U-Pb zircon age
Triassic
Griesbachian
Daye
Permian
Changhsingian
Talung
FO H. parvus
POT 68T
251.64 ± 0.130
POT 67T
251.668 ± 0.079
POT 66T
251.589 ± 0.052
LAX 10T
251.822 ± 0.060
LAX 8T
252.07 ± 0.130
5 m
PTB
A
B
C
D
E
F
G
0 15 30
Al (wt.%)
0 20 40
Hg/Al
0 20 40 60
Hg/Fe
0 100 200
Hg/TOC (ppb/wt.%)
0 2 4 6
Mo/Al
0 5.0
U/Al
−2 −1 0
δ202Hg (‰)

Figure 6.

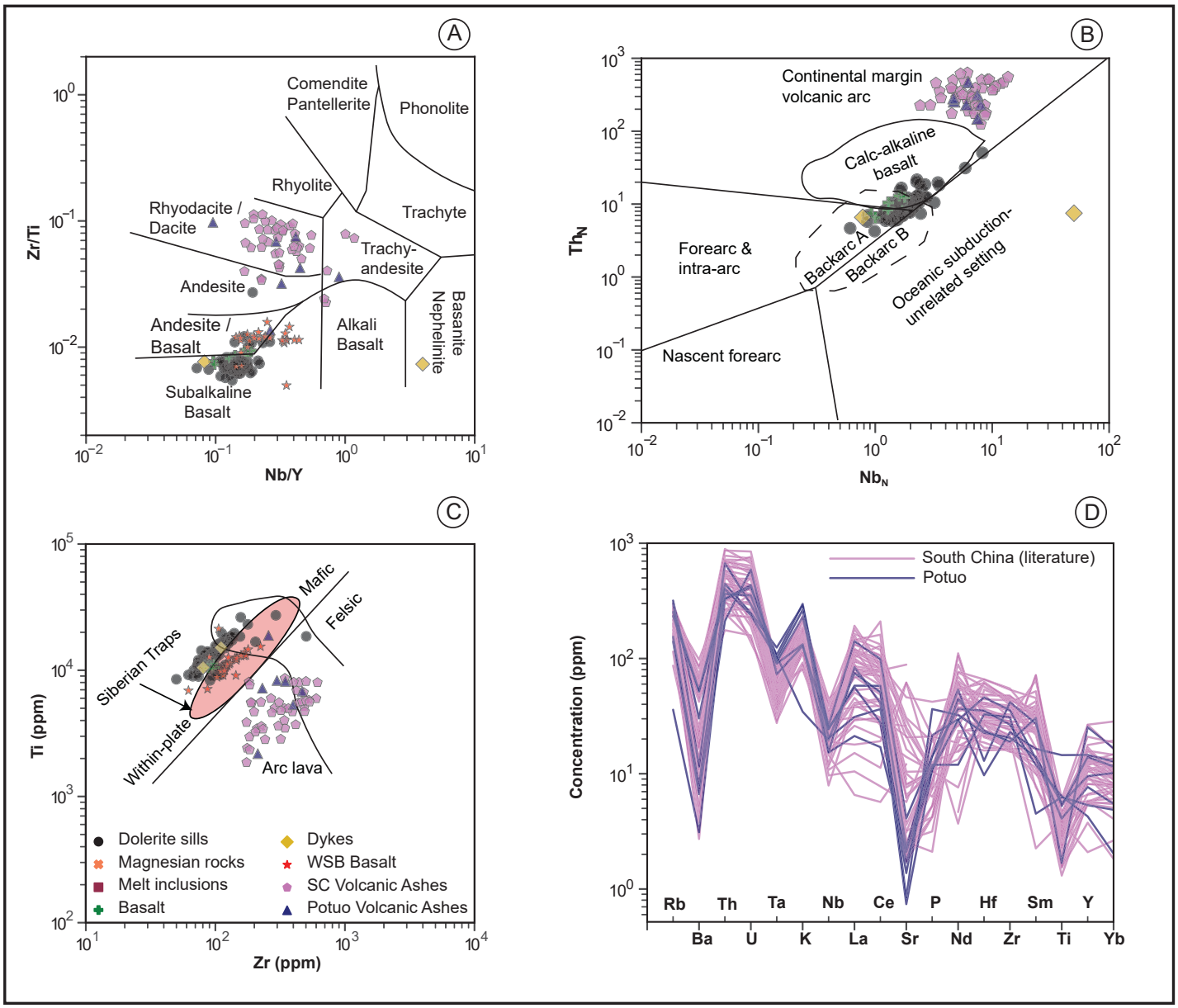
A
Comendite
Pantellerite
Phonolite
Rhyolite
Trachyte
Rhyodacite /
Dacite
Trachy-
andesite
Andesite
Andesite /
Basalt
Alkali
Basalt
Basanite
Nephelinite
Subalkaline
Basalt
Zr/Ti
Nb/Y
B
Continental margin
volcanic arc
Calc-alkaline
basalt
Forearc &
intra-arc
Backarc A
Backarc B
Oceanic subduction-
unrelated setting
Nascent forearc
Th_N
Nb_N
C
Mafic
Felsic
Siberian Traps
Within-plate
Arc lava
Dolerite sills
Magnesian rocks
Melt inclusions
Basalt
Dykes
WSB Basalt
SC Volcanic Ashes
Potuo Volcanic Ashes
Ti (ppm)
Zr (ppm)
D
South China (literature)
Potuo
Concentration (ppm)
Rb
Th
Ta
Nb
Ce
P
Hf
Sm
Y
Ba
U
K
La
Sr
Nd
Zr
Ti
Yb

Figure 7.

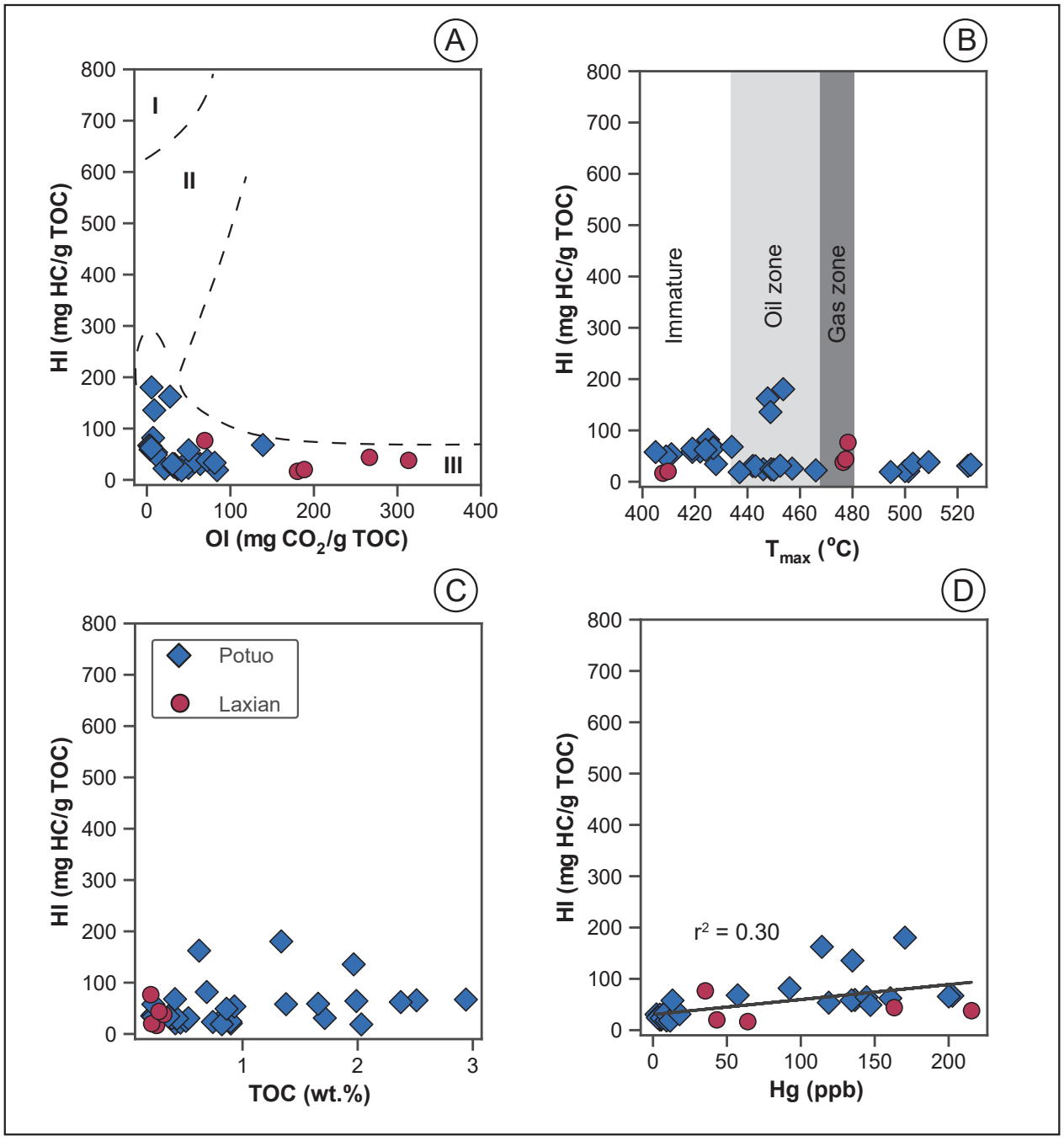
A
B
C
D
I
II
III
HI (mg HC/g TOC)
OI (mg CO2/g TOC)
Immature
Oil zone
Gas zone
Tmax (°C)
Potuo
Laxian
TOC (wt.%)
r2 = 0.30
Hg (ppb)

Figure 8.

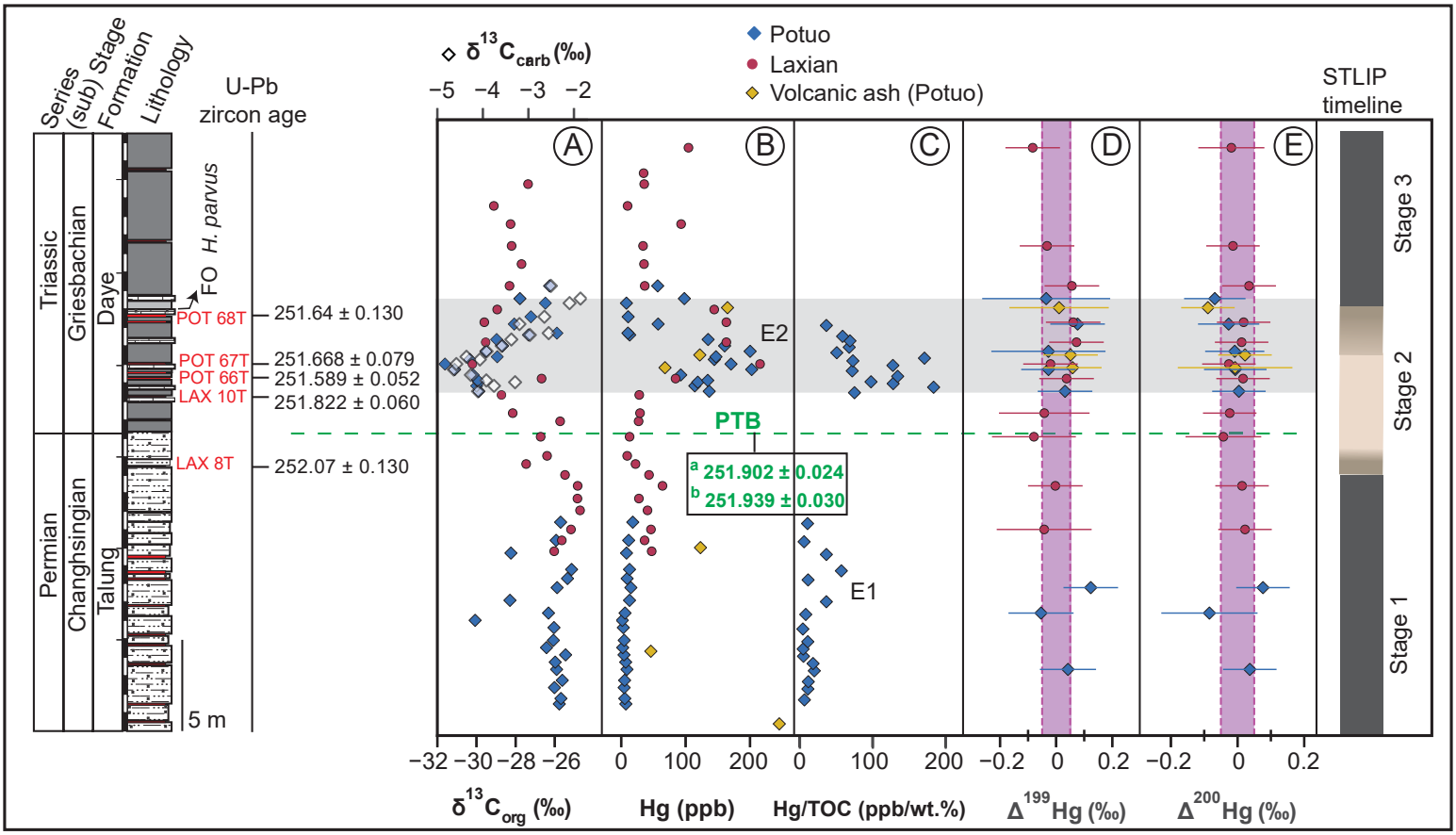
Series
(sub) Stage
Formation
Lithology
U-Pb
zircon age
Triassic
Griesbachian
Daye
Permian
Changhsingian
Talung
H. parvus
FO
POT 68T
POT 67T
POT 66T
LAX 10T
LAX 8T
251.64 ± 0.130
251.668 ± 0.079
251.589 ± 0.052
251.822 ± 0.060
252.07 ± 0.130
5 m
δ13Ccarb (‰)
Potuo
Laxian
Volcanic ash (Potuo)
STLIP
timeline
A
B
C
D
E
E2
E1
PTB
a 251.902 ± 0.024
b 251.939 ± 0.030
Stage 3
Stage 2
Stage 1
δ13Corg (‰)
Hg (ppb)
Hg/TOC (ppb/wt.%)
Δ199Hg (‰)
Δ200Hg (‰)

Figure 9.

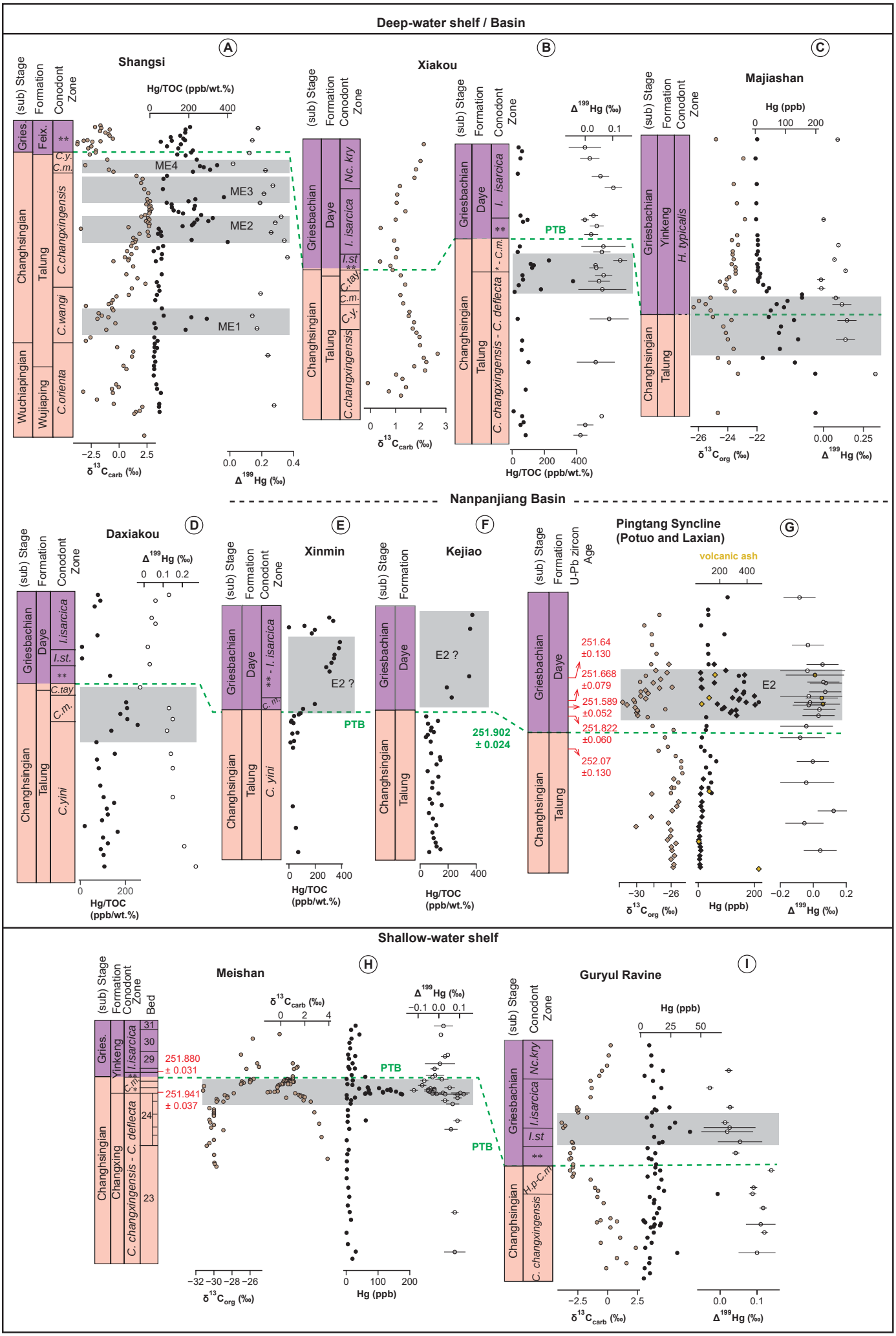
Deep-water shelf / Basin
A
Shangsi
B
Xiakou
C
Majiashan
Nanpanjiang Basin
D
Daxiakou
E
Xinmin
F
Kejiao
G
Pingtang Syncline (Potuo and Laxian)
Shallow-water shelf
H
Meishan
I
Guryul Ravine
(sub) Stage
Formation
Conodont Zone
Bed
U-Pb zircon Age
Hg/TOC (ppb/wt.%)
Hg (ppb)
Δ199Hg (‰)
δ13Ccarb (‰)
δ13Corg (‰)
ME1
ME2
ME3
ME4
PTB
E2
E2 ?
volcanic ash
251.64 ±0.130
251.668 ±0.079
251.589 ±0.052
251.822 ±0.060
252.07 ±0.130
251.902 ± 0.024
251.880 ± 0.031
251.941 ± 0.037